Facultad de Ciencias

SYSTEMATIC STUDY OF THE COLOR OF COLLOIDS OF METALLIC NANOPARTICLES
(ESTUDIO SISTEMÁTICO DEL COLOR DE COLOIDES DE NANOPARTÍCULAS METÁLICAS)

Trabajo de Fin de Máster
para acceder al

MÁSTER EN FÍSICA, INSTRUMENTACIÓN Y MEDIO AMBIENTE

Autor: Elena de la Hoz López-Collado

Director\es: Francisco González Fernández
Rodrigo Alcaraz de la Osa

Septiembre - 2018

ABSTRACT

Metallic nanoparticles under electromagnetic radiation illumination experience physical phenomena known as localized plasmon resonances whose most significant consequence is a great enhancement of the electric field in the vicinity of the nanoparticles. These phenomena are responsible for stunning colorimetric properties of certain metallic nanoparticles colloids. However, the relationship between the colloids properties and their color is neither simple nor direct. In this work we review how color coordinates can be evaluated from colloids properties. There are three aspects involved in color coordinates calculations: i. localized plasmon resonances, ii. radiative transfer models, and iii. color science. Here, we have studied each one of them independently, and applied them in combination to study colloids' color dependences on nanoparticles size, shape, optical properties, and the embedding medium. Additionally, we have developed a multilayer four-flux based Monte Carlo to study light transfer. This Monte Carlo, unlike analytical methods, allows the study of transient states, and light transfer across heterogeneous media. The color review conducted in this work has, among others, potential applications in industries where coloring techniques are applied, e.g., glass industry.

Keywords: color, metallic nanoparticles, light transfer, four-flux, localized plasmon resonances

RESUMEN

Cuando nanoparticulas metálicas son iluminadas con radiación electromagnética sufren fenómenos físicos conocidos como resonancias plasmónicas localizadas cuya principal consecuencia es un aumento signficativo del campo eléctrico en las inmediaciones de las nanopartículas. Estas resonancias son responsables de las sorprendentes propiedades colorimétricas de algunos coloides de nanopartículas metálicas. Sin embargo, la relación entre las propiedades de los coloides y su color no es simple ni directa. En este trabajo, se ha revisado como obtener coordenadas de color a partir de las propiedades de los coloides. Hay tres aspectos involucrados en estos cálculos: i. resonancias plasmónicas localizadas, ii. modelos de transfencia de radiación, y iii. la ciencia del color. En este trabajo se ha estudiado cada uno de estos aspectos de forma independiente, y se han aplicado en conjunto en el estudio de la dependencia del color de los coloides en función de las propiedades ópticas, tamaño y forma de las nanopartículas, y del medio embebedor. También, se ha desarrollado un Monte Carlo multicapa basado en el "four-flux model" para estudiar el transporte de luz. Este Monte Carlo, al contrario que modelos analíticos, permite estudiar estados transitorios además de medios heterogéneos. El análisis del color realizado en este trabajo tiene, entre otras, una potencial aplicación en industrias que utilicen técnicas de coloreado, por ejemplo en la industria del vidrio.

Palabras clave: color, nanopartículas metálicas, transferencia de luz, four-flux, resonancias plasmónicas localizadas

ACKNOWLEDGEMENTS/AGRADECIMIENTOS

Me gustaría agradecer y reconocer la contribución, tanto en el ámbito académico como en el personal, a todas las personas que me han ayudado en el transcurso de este trabajo. Sin vosotros este año no hubiese sido igual.

Primero de todo, me gustaría agradecer a Paco y muy en especial a Rodri por haberme dirigido en el desarrollo de este trabajo. Ha sido todo un placer poder trabajar con vosotros.

Al grupo de Óptica, por enseñarme indirectamente valiosas lecciones de la vida que se escapan del ámbito académico.

A mis compañeros y amigos, por estar siempre ahí tanto en los buenos como en los malos momentos. En especial, quiero agradecerle a Fer todo su apoyo, sobretodo por escucharme (aguantarme) cuando he necesitado desahogarme. Te mereces un monumento.

Por último y no por ello menos importante, a papá, a mamá, a Isa, a Car y a Kiko. Vosotros sois el pilar de mi vida. Os quiero muchísimo.

CONTENTS

CHAPTER 1

INTRODUCTION

The present work is focused mainly on the colorimetric properties of metallic nanoparticles. Therefore, this opening chapter aims to introduce the reader to: i. relevant aspects of metallic nanoparticles such as the explanation of the physical phenomena that make them versatile, several synthesis techniques, and current and potential applications of them; and ii. the relationship between the color of metallic nanoparticles colloids and their properties.

Metallic nanoparticles (NPs)[1] have numerous applications in a wide range of fields such as biomedicine, environmental sciences, optical computation, etc. When light is shined on them, phenomena such as localized surface plasmon resonances, a.k.a., localized plasmon resonances (LPRs), occur. These resonances yield an enhancement of the electromagnetic field in the NPs surroundings, in regions smaller than the wavelength of the incident radiation. The presence of these resonances depends on NPs optical properties, shape, size, the wavelength of the incident radiation, the medium where the NPs are embedded, etc.

In the last few decades, a collection of different techniques to synthesis metallic NPs with specific characteristics, such as size, shape, etc. were developed with successful results. The wide variety of NPs available opened the door to the search of optimal metallic NPs in different potential applications of these versatile NPs, e.g., spectroscopy, photocatalysis, sensing, optical computation, etc.

Many metals have LPRs in the visible spectral range which result in astonishing colorimetric characteristics. However, determining the color of metallic NPs from their properties is not straightforward. Color is itself an intricate magnitude. It involves the spectral characteristics of three different factors: the object subject to be observed, in this case the metallic NPs colloids[2]; the type of light that illuminates them; and the observer. Likewise, there are other elements that have to be taken into account in the evaluation of the aforementioned aspects. To set out this relationship in an insightful manner we provide, in this chapter, a simple outline of how color and NPs colloids properties are related.

This chapter is organized in two sections. Section 1.1 covers several aspects related to

[1] In the following the term NPs will refer only to metallic NPs.

[2] A colloid is defined as "a solid, liquid, or gaseous substance made up of very small, insoluble particles (as single large molecules or masses of smaller molecules) that remain in suspension in a surrounding solid, liquid, or gaseous medium of different matter" [1].

metallic NPs, in particular, the origin of LPRs, modern synthesis techniques, and practical applications of them. Finally, section 1.2 presents schematically how metallic NPs properties and their color are related and outlines the organization of the rest of the work.

1.1 Metallic Nanoparticles

Metallic NPs are small entities whose size ranges from a few nanometers to several hundreds. They can be composed of pure metals like gold or silver, or their compounds, such as oxides, hydroxides, sulfides, phosphates. In the last century NPs have received special attention from the scientific community due to their potential applications, which arise from LPRs that occur in the NPs vicinity.

In this section we explain the physical phenomenon of LPRs, mention some modern NPs synthesis techniques and give some examples of NPs applications.

1.1.1 Localized Plasmons Resonances

LPRs are a physical phenomenon that occurs when metallic NPs are shined on with an electromagnetic field whose wavelength (λ) is larger than the NPs size. [3] The driving field collectively excites the conductive electrons of the NPs generating coherent localized plasmon oscillations which results in an enhancement of the electromagnetic field in the NPs surroundings.

In the case of metallic NPs whose size is much smaller than λ, the incident field is approximately constant over the whole NPs extension. Therefore, the conduction electrons follow the driving field in phase. This leads to the accumulation of polarization charges on the surface of the NPs. The positively-charged nuclei generates an effective restoring force on the driven electrons which allows a resonance to occur at a certain frequency. The resonance occurs when there is a $\pi/2$ phase shift between the incident field and electrons oscillations. The resonant frequency is highly dependent on the the NPs optical properties, size, shape, and the dielectric embedding. A simple diagram of this phenomenon is shown in fig. 1.1.

This resonance leads to a field amplification inside the NPs, as well as a generation of a dipolar field in the neighboring area outside the NPs. This results in an enhancement in the absorption and scattering cross-sections in addition to an enhanced electromagnetic field in the surroundings of the NPs surfaces.

For larger particles the spectral response is modified due to: i. retardation effects, i.e., the approximation of constant incident field does not hold anymore, and ii. the excitation of higher-order modes (quadrupole, octopole,...).

1.1.2 Metallic Nanoparticles Synthesis

There are many diverse synthesis techniques, but they can be cataloged as either bottom-up or top-down methods. In the former, NPs are generated by piecing together smaller

[3] Comprehensive reviews on LPRs are provided in [2], [3] and [4].

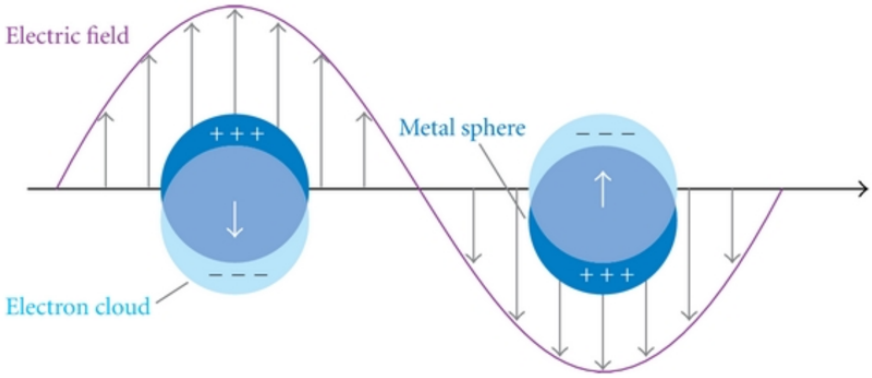

Figure 1.1: Scheme of conduction electron oscillations when the resonant condition is satisfied ($\pi/2$ phase lag between the electron oscillations and the incident electromagnetic field). The figure has been retrieved from [5].

components, e.g., molecules, atoms, to build up more complex systems, while, in the later, external controlled tools are used to mold bulk materials into the desired shape.

In the following we highlight a few methods among the extensive list of synthesis techniques. Reviews of the metallic NPs synthesis methods are given in [6] and [7].

Bottom-up Methods

- *Seed mediated synthesis*: Small seed particles are placed in a solution with reducing agents to promote the seed growth. The type of reducing agents used enable the control of the final shape and size. In chapter 5, we study how the size distribution of NPs synthesized with this method affects the final color of NPs colloids.
- *Biosynthesis*: Bacteria, fungi and other organic compounds, in the presence of some precursors, can produce NPs. This represents a more environmentally friendly substitute of conventional chemical reactions.

Top-down Methods

- *Electron-beam lithography*: A focused beam of electrons scans a surface covered with an electron-sensitive film in order to create custom shapes. The main advantage of this technique is that the drawn patterns are well resolved even below the 10 nm range.
- *Mechanical milling*: A powder of the compound of interest is placed in a high energy mill, along with a suitable milling medium. The size of the particle is reduced by recurrent impacts with the milling medium, e.g., balls. This technique also permits the blending of particles in new phases.

1.1.3 Metallic Nanoparticles Applications

The recent interest in metallic NPs arises mainly due to their potential applications. Here some of their most significant applications are outlined.

- *Photocatalysis*: Catalysis is the process by which the rate of a chemical reaction is increased by the addition of a substance or catalyst. Catalysis has many applications, e.g., reduction of industrial time processes, transformation of hazardous products into inert ones, etc. Some metallic NPs exhibit catalytic activity which can be enhanced by the excitation of LPRs. Under electromagnetic radiation, pairs of electron/holes are created by the promotion of electrons from the valence to the conduction band. The excited electrons contribute to oxidation reactions while holes facilitate reduction reactions. [8]

- *Surface Enhanced Raman Scattering (SERS)*: SERS is a technique used to detect diverse molecules from its Raman scattering. Raman scattering is commonly weak but the use of metallic NPs make this tool effective since it increases the Raman intensity by several orders of magnitude. To amplify the Raman signal, the molecules are placed over nanoscale roughened metal surfaces. Upon illumination, these metal nanostructures resonantly generate a highly localized plasmonic field. The enhanced field at the surface leads to a large enhancement in the Raman signal of neighboring molecules. [9]

- *Solar Energy*: Nowadays, solar energy is regarded as one of the most powerful alternatives to traditional environmentally harmful energy sources, e.g., energy sources based on fossil fuels. However, the current technology has very low conversion efficiencies from solar light into electrical power. The addition of metallic NPs to solar cells helps to concentrate and enhance the solar electric field inside them, which could potentially increase the efficiency of solar panels. [10]

1.2 Color of Metallic Nanoparticles

As mentioned previously, the relationship between the NPs colloids properties and their color is indeed very complex. Therefore, in order to aid the reader, in this section we explain step wisely how the color coordinates of metallic NPs colloids can be calculated. Figure 1.2 shows a scheme of the steps to be taken.

There are three aspects involved in color perception: the observed object, the illuminant source, and the observer. Thus, to calculate color coordinates we need the source's, the object's, and the observer's spectral response. While the spectral characteristics of the source and the observer have been standardized by an international authority on light, illumination, color and color spaces; the Commission Internationale de l'Eclairage (CIE), the spectral characteristics of the observed object depend greatly on the object's response to the electromagnetic field.

The object's response, which can be expressed with macroscopic magnitudes such as the spectral transmittance or reflectance, can be obtained from radiative transfer models. These models describe light propagation in physical media. From the frequency-dependent optical properties of a material, i.e., the spectral scattering and absorption coefficients, we can obtain both macroscopic magnitudes.

The spectral scattering and absorption coefficients of the colloids under study strongly depend on the LPRs characteristics. LPRs can be evaluated using light scattering theories

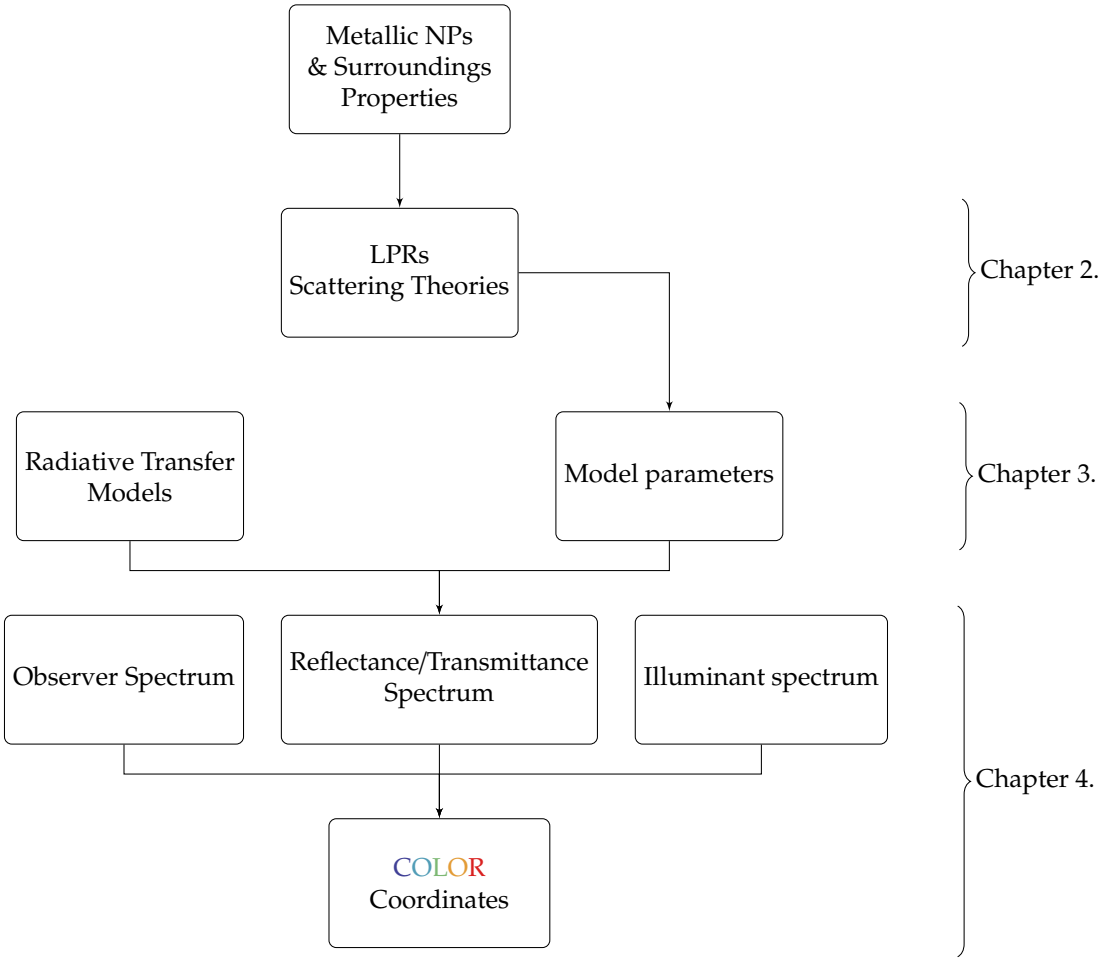

Figure 1.2: Diagram with the different stages involved in color calculations. On the right side it is shown the chapter that covers the selected stage.

once the NPs and their surroundings' properties are known. Thus, following backwards these instructions, we can calculate the color coordinates of metallic NPs colloids from their properties.

Taking into account the previous comments, we require further knowledge of LPRs, radiative transfer models, and color science, in order to evaluate the color of metallic colloids. These topics are covered in chapter 2, chapter 3 and chapter 4 respectively. Then, in chapter 5 we study the color dependence of NPs colloids on the NPs optical properties, size, shape, and the dielectric embedding medium. Finally, chapter 6 summarizes and highlights the takeaways of the present work.

CHAPTER 2

LOCALIZED PLASMON RESONANCES

The spectral scattering and absorption coefficients needed to evaluate the colloids' spectral response (involved in color coordinates calculations) are directly related to LPRs. The spectral behavior of LPRs can be analyzed from light scattering theories and colloids' properties. In this chapter we use these theories to study how LPRs vary as a function of the NPs optical properties, their size, shape and the embedding medium.

Light scattering is the phenomenon produced when light interacts with an obstacle, such as an electron, an atom or a solid particle. With regard to the energy transfer there are two types of scattering: elastic, when the energy transfer is negligible, and inelastic scattering. Examples of inelastic scattering are Raman or Compton scattering [11]. In this chapter we focus only on elastic scattering since it is the one that affects our metallic NPs [12].

The relative size of the obstacle with respect to the wavelength of the incident radiation plays a major role in the interaction. The relative size is characterized by the size parameter

$$x = \frac{2\pi r n_{sm}}{\lambda}, \tag{2.1}$$

where r is the NPs radius, n_{sm} is the refractive index of the surrounding medium and λ is the wavelength of the incident radiation. According to the value of x we can distinguish three regimes

- When $x \ll 1$, also known as the small particle limit. In this regime NPs feel an approximately constant field in their whole extension. In the case of metallic NPs, conductive electrons oscillate in phase which leads to the generation of a dipole electric field in the NPs surroundings.
- When $x \sim 1$, particles size are of the order of the incident wavelength and hence the assumption of approximately constant electric field over the whole particle extension does not hold anymore. Gustav Mie developed in 1908 an scattering theory for spherical particles of any x in order to explain surprising colorimetric properties of metallic spherical particles, in particular, the color effects of gold colloids [13]. Although there is no general theory there have been several extensions [14].
- When $x \gg 1$, which corresponds to the limit where geometric optics apply. Light propagation can be described in terms of rays, i.e., imaginary perpendicular to the wavefronts lines useful in approximating the paths along which light propagates.

Since we are interested in studying nanoparticles in the visible part of the electromagnetic spectrum we are interested in the theories where $x \sim 1$. In this work we have studied LPRs using Mie theory, in the case of spherical NPs, and the T-matrix method (an extension of Mie theory) in the case of spheroidal NPs. Both formalisms are reviewed in appendix A.

The chapter is organized in two sections. In section 2.1 we define the relevant physical magnitudes used to characterize LPRs, and in section 2.2 the mentioned theories are used to study LPRs as a function of NPs optical properties, size, shape, and the refractive index of the surrounding medium.

2.1 Physical Magnitudes

The strength of LPRs can be studied from extinction, scattering and absorption **cross sections** defined as the net rate at which electromagnetic energy is extinguished, scattered or absorbed by a particle with respect to the incident radiation.

The relative amount of electromagnetic radiation absorbed, scattered or extinguished can also be expressed in terms of dimensionless magnitudes, e.g., the **efficiency factors** Q. The efficiencies are related to the cross sections as

$$Q = \frac{C}{G}, \tag{2.2}$$

where G is the particle cross-sectional area projected onto a plane perpendicular to the incident beam. Particularly, in the case of a sphere with radius r, $G = \pi r^2$.

Another relevant magnitude related to LPRs is the spatial distribution of the scattered field. This can be studied from the **phase function** which specifies the angular distribution of the scattered light, i.e., the amount of light scattered into a unit solid line in a given direction. A mathematical definition of the phase function is provided in eq. (A.27).

2.2 LPRs Variations

In this section we study the spectral behavior of LPRs originated by metallic NPs colloids as a function of: NPs optical properties, section 2.2.1; NPs size, section 2.2.2; refractive index of the surrounding medium, section 2.2.3; and the aspect ratio of spheroidal NPs, section 2.2.4.

2.2.1 Metallic NPs Optical Properties

The LPRs spectral shape and position depend greatly on the optical properties of the NPs, i.e., the frequency-dependent dielectric function ϵ, or equivalently the spectral complex refractive index. As a consequence, some metallic NPs may be more suitable than others in a particular application. The suitability of the different NPs is determined mainly by the spectral characteristics of their LPRs, and other NPs properties such as oxidation susceptibility, catalytic activity, toxicity, etc. There are several reviews in the literature that compares the plasmonic capabilities of different materials [15], [16].

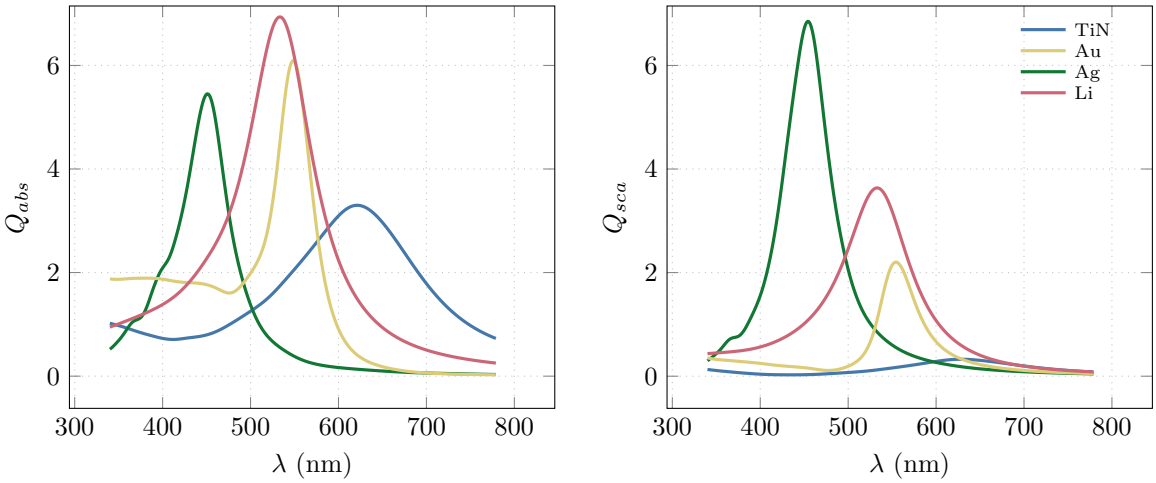

Figure 2.1: Spectral absorption and scattering efficiencies of different metallic NPs with radii $r = 25$ nm, embedded in glass ($n_{sm} = 1.5$).

To exemplify the LPRs dependence on NPs optical properties, we have evaluated[1] the spectral absorption and scattering efficiencies, $Q_{abs}(\lambda)$ and $Q_{sca}(\lambda)$, of four diverse metals with LPRs within the visible spectrum, in particular Ag, Au, TiN and Li. We have chosen metals with LPRs in the visible since they will have a drastic effect on the color perceived. In the calculation we have fixed the NPs radii to be $r = 25$ nm, the refractive index of the surrounding medium $n_{sm} = 1.5$ (a glass), and use the bulk optical constants from [17].[2] The results are shown in fig. 2.1.

We observe in fig. 2.1 that not only does the resonant frequency peak at different wavelengths, but also the band width and intensity of the LPRs are substantially different. These variations will result in large color differences as it will be seen in chapter 5. In the case of Au NPs we also notice that there is a flat contribution to the Q_{abs} at shorter wavelengths. This contribution is not a result from LPRs, but from interband transitions. The most distinctive characteristic of a metal is that the conduction and valence bands overlap creating a continuum spectrum of states. Nonetheless, there might be some inner levels spread over only the valence band. Thus, interband transitions between these levels and the conduction band can occur. These transitions are very rare in bulk materials but show up at the nanoscale range in metals like Au.

2.2.2 Size

The NPs size is another crucial factor that affects the LPRs characteristics. LPRs size dependence can be split up into two regimes with regard to the NPs size range, a small NPs regime ($x \ll 1$) and a large NPs regime ($x \lesssim 1$).

In the small NPs regime the size parameter is $x \ll 1$ and the predominant contribution arises from the dipole mode. As size is progressively increased, both LPRs intensity and

[1] With the miescattering code provided in appendix B.

[2] Although there is a size lower limit from which bulk constants no longer apply due to quantum effects, the assumption of bulk optical constants for particles larger than 50 Å is reasonable [18]

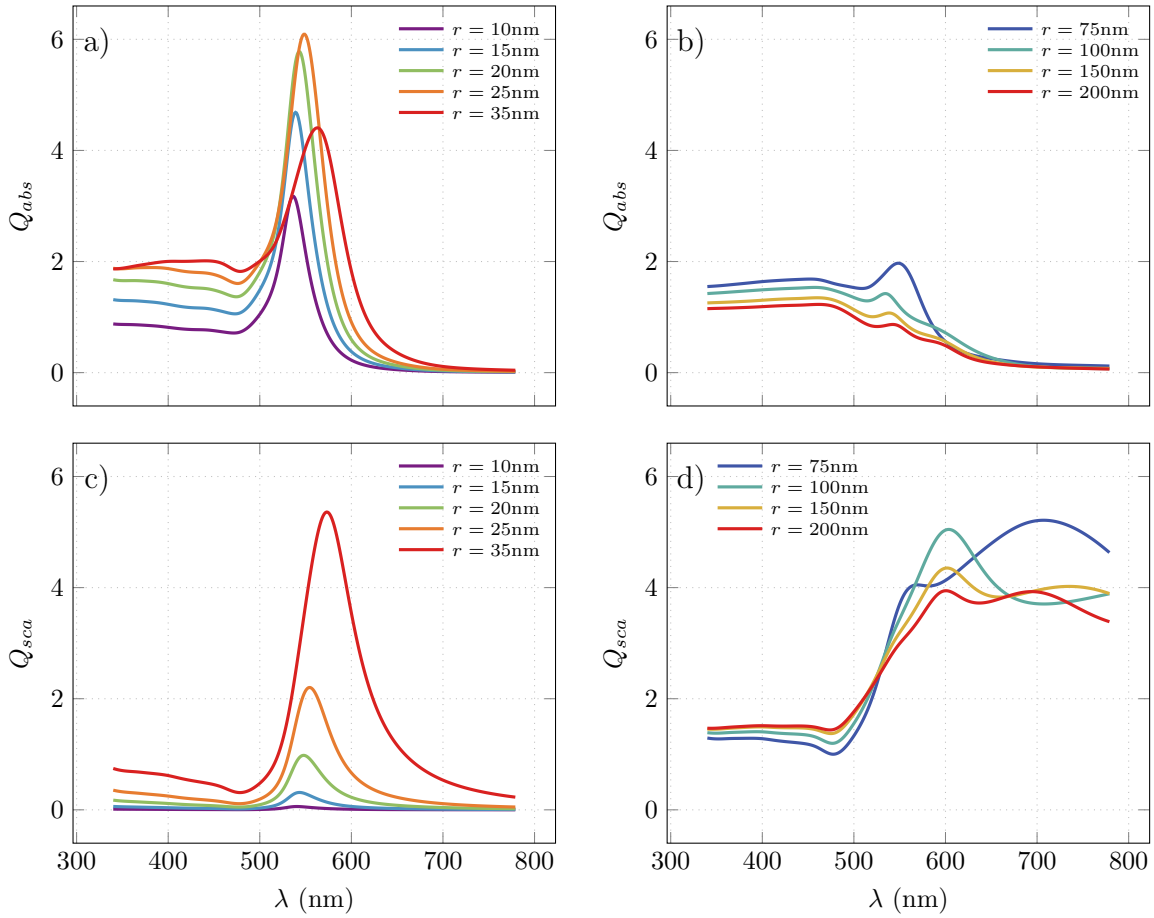

Figure 2.2: Spectral absorption and scattering efficiencies of spherical Au NPs, embedded in glass (n_{sm} = 1.5), with different radii.

width increase. These effects can be understood if the electron dipole oscillations are modeled as a linear oscillator. The electron oscillations are damped due to the scattering with the ionic core and with the surface. The former is size-independent unlike the latter [3]. An increase in the particle size yields a decrease in the fraction of electrons at the surface which results in a decrement of the total damping. Increasing the damping in linear oscillator results in a reduction of the intensity and an increment of the width of the LPRs. On the other hand, the resonant frequency suffers a small red-shift. Those are the effects observed on fig. 2.2 a) and c) which shows the spectral absorption and scattering efficiencies of spherical Au NPs with different radii within this regime. Another essential aspect worth mentioning is that, in this regime, Q_{abs} dominates over Q_{sca}.

When the NPs are extremely small ($r < 5$ nm [18]), quantum phenomena arises and the dielectric function becomes size-dependent, and the bulk optical properties no longer apply. We have not studied such small NPs, and we have assumed bulk optical constants in all the calculations.

In the large NPs regime larger multipolar contributions have to be considered. Every multipolar term contributes with a peak at a different resonant frequency, [3]. The total

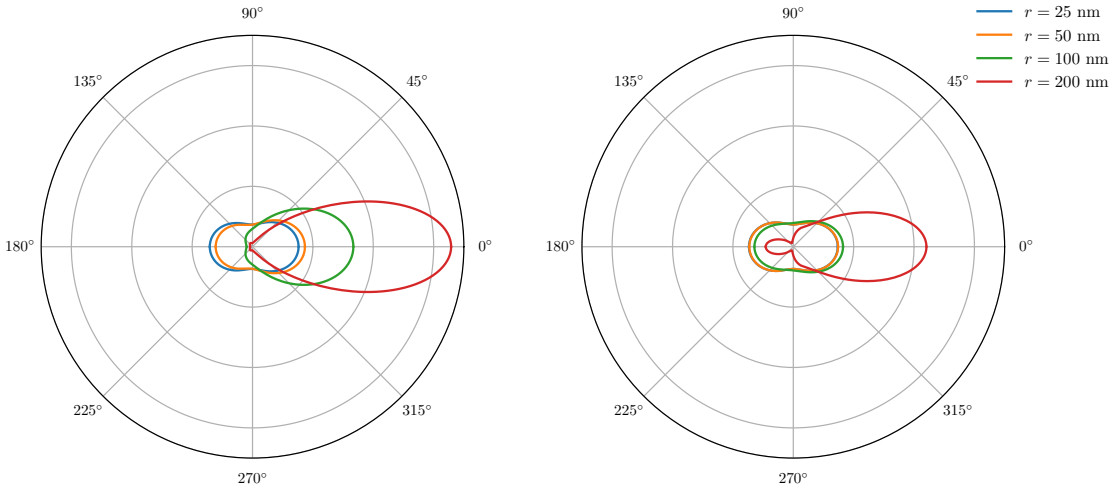

(a) $\lambda = 440$ nm (b) $\lambda = 590$ nm

Figure 2.3: Angle-dependent phase functions of spherical Au NPs, embedded in glass ($n_{sm} = 1.5$), with different radii under two different monochromatic illuminations: (a) λ =440 nm; and (b) λ =590 nm.

spectral efficiencies represent the sum of the efficiency spectrum of each mode. Therefore multiple peaks can appear in them as it can be observed on fig. 2.2 b) and d). If the size is further increased the LPRs cannot be considered as the sum of the contributions of individual modes. Instead, collective effects appear and the LPRs phenomenon is averaged out.

Another size-dependent factor is the angular distribution of the scattered intensity, which can be examined using the phase function. In fig. 2.3 we show the normalized phase function of spherical Au NPs, with different radii, within a glass surrounding, when shined on with two different λ.

As can be seen from fig. 2.3 the phase function depends on the relative size of the NPs with respect to incident light, i.e., on the size parameter x. We observe that for large x there is significantly more forward scattering, while the smaller x, the more isotropic the scattering field is. The former can be understood analyzing the limiting case of geometric optics $x \gg 1$. In this case, the amount of light scattered back is simply the light reflected. From Fresnel reflectance factors we see that the relative reflected light is very small and almost negligible for transparent media. As an example, consider the reflectance at normal incidence of a glass sphere embedded in air

$$R = \left|\frac{n_a - n_g}{n_a + n_g}\right|^2 = \left|\frac{1 - 1.5}{1 + 1.5}\right|^2 \sim 0.04\,.$$

As it mentioned before, when $x \ll 1$ the LPRs lead to the creation of a dipolar field in the surrounding area. The polarization of the dipole field induced is in the same direction as the incident field. When the system is shined with unpolarized light the scattered field is the average of a collection of dipole fields in random directions and is approximately isotropic.

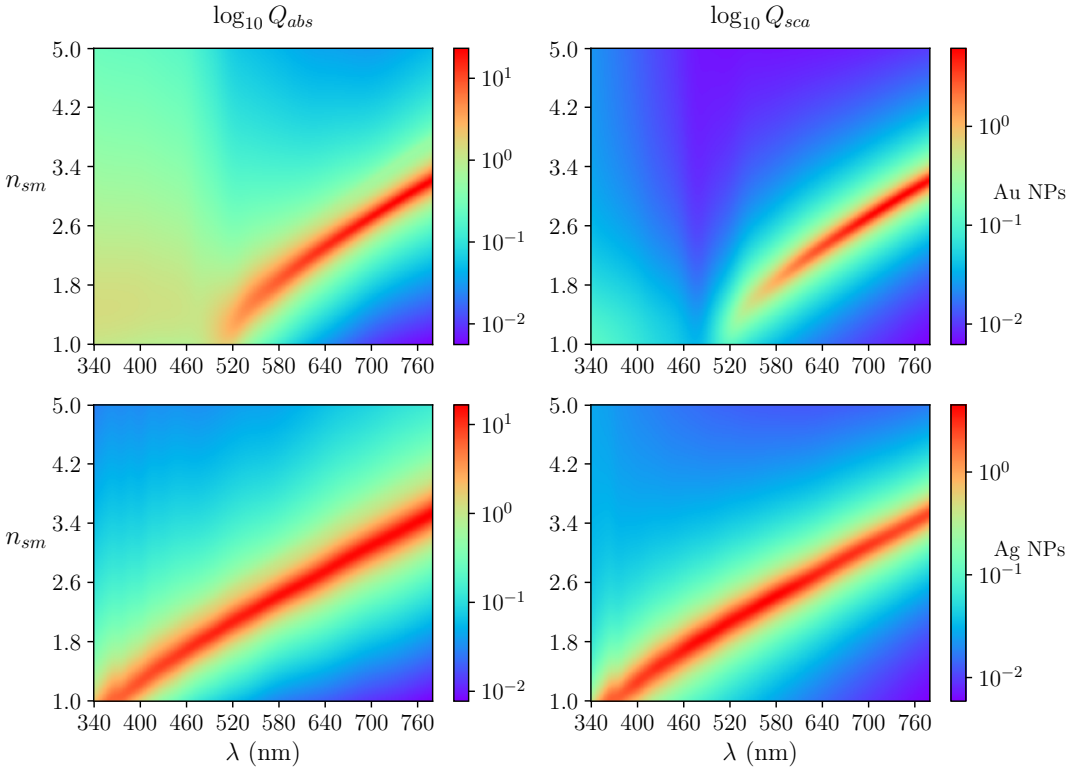

Figure 2.4: Spectral absorption (left panels) and scattering (right panels) efficiencies as a function of a medium's refractive index with gold (top panels) or silver (bottom panels) NPs inclusions, $r = 25$ nm. The efficiencies are given in logarithmic scale to enhance the contrast.

2.2.3 Dielectric Embedding Medium

LPRs are greatly influenced by the surrounding media in which the NPs are embedded. The LPRs medium dependency emanate from the medium being susceptible to become polarized.

LPRs induce an electric field in the vicinity of the NPs which polarizes the embedding medium. This polarization yields a charge accumulation at the interface between the NPs and their surroundings which reduces the movement of the conduction electrons, i.e., it reduces the oscillating electrons' restoring force. The larger the refractive index of the embedding medium, the larger the charge accumulation, hence a larger reduction of the restoring force. A decrement in the restoring force leads to a shift of the resonant frequency toward smaller frequencies, or equivalently, a red-shift of the wavelength. A more comprehensive explanation of this effect can be found in [3].

Figure 2.4 shows the spectral absorption and scattering efficiencies as a function of the refractive index of the embedding medium[3] of spherical Au and Ag NPs of size $r = 25$ nm. We observe a red-shift with increasing embedding medium's refractive index in both gold and silver colloids as it was expected. We also notice that at $n_{sm} \gtrsim 3.5$, the LPRs resonant frequencies are no longer in the visible spectrum for both Au and Ag NPs.

[3]Only non-absorbing embedding media have been analyzed in the present work.

2.2.4 Shape. Spheroids

The shape of NPs, e.g, spherical, cubical, etc. can dramatically change the characteristics of the LPRs of a given material [2]. In this work we have restricted to the study of spheroids, 3-D particles whose shape is obtained by rotating an ellipse about one of its principal axes, i.e., an ellipsoid with two equal semi-diameters. If the ellipse is rotated about the minor (major) axis the spheroid is oblate (prolate), see fig. 2.5a (fig. 2.5b).

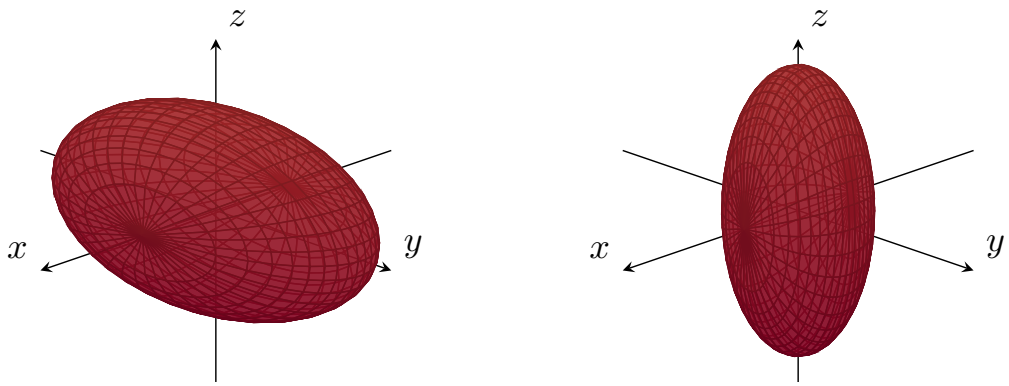

(a) Oblate (b) Prolate

Figure 2.5: Spheroids

The equation of a spheroid is

$$r(\theta) = \frac{ac}{\sqrt{a^2\cos^2\theta + c^2\sin^2\theta}} \tag{2.3}$$

where a is the semi-axis length along the x and y-axes, and c is the semi-axis length along the z-axis. The aspect ratio, η, of a spheroid is the ratio of the z semi-axis to either the x or y semi-axes length:

$$\eta = \frac{c}{a}, \tag{2.4}$$

and is used to characterize the spheroids. Oblate (prolate) spheroids have $\eta < 1$ ($\eta > 1$). Another magnitude useful to characterize spheroids is the volume-equivalent radius r_V. r_V is the radius of a sphere with the same volume as the particle. Thus, for a spheroid

$$r_V = \sqrt[3]{a^2 c}, \tag{2.5}$$

Unlike spheres, spheroids are not completely symmetrical and therefore the incident direction and polarization of the electric field becomes relevant. When linearly polarized light in the z-direction interacts with the spheroid, it "feels" an effective cross-section equivalent to that of a sphere of radius c. On the other hand, when the incident radiation is polarized along the x or y-direction, it responds as if it were interacting with an effective sphere of radius a. In the case of unpolarized light the response is the average of all possible polarization directions.

In order to study this effect we have evaluated[4] the absorption and scattering cross sections of an oblate ($\eta = 0.5$) and a prolate spheroid ($\eta = 2$) with $r_V = 25$ nm illuminated with linearly polarized light and unpolarized light. The results are shown in fig. 2.6.

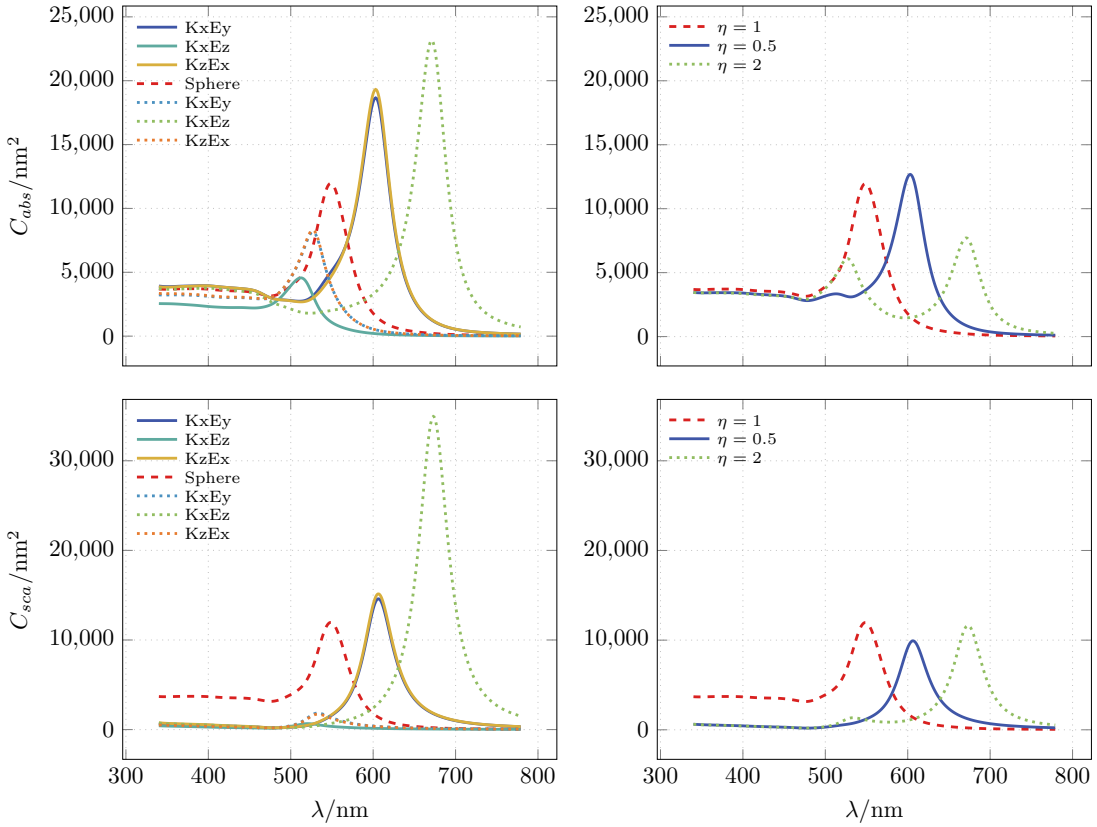

Figure 2.6: Spectral absorption and scattering cross sections of gold colloids in a glass embedding ($n_{sm} = 1.5$). The Au NPs are spheroids of $r_V = 25$ nm with different aspect ratios $\eta = 0.5$ (oblate, solid lines), η (sphere, dashed lines) and $\eta = 2$ (prolate, dotted lines). The semi-axis lengths of the oblate (prolate) spheroid are $a \simeq 32$ nm and $c \simeq 16$ nm ($a \simeq 20$ nm and $c \simeq 40$ nm).

Let us analyze the results when the system is under polarized light illumination (left panels of fig. 2.6). For the oblate spheroid, we observe that the cross sections are larger when the electric field is polarized along the x or y-direction instead of the z-direction, and vice versa for the prolate spheroid. As we saw in section 2.2.2, in the small particle regime, an increase in the effective radius yields larger absorption and scattering efficiencies. The larger the effective sphere the incident light experiences, the larger the cross-sections.

When the system is illuminated with unpolarized light (right panels of fig. 2.6) we observe that the spectral cross-sections shows two peaks, one blue-shifted and the other red-shifted with respect to the spherical case. These peaks arise from the two different semi-axis lengths. Smaller (larger) radii lead to a blue-shift (red-shift). The prolate spheroid shows a larger blue-shifted peak than the oblate. This happens because there are more polarization directions that "sees" a smaller effective sphere.

[4]We have used an open-source suite of MATLAB codes called SMARTIES (Spheroids Modeled Accurately with a Robust T-matrix Implementation for Electromagnetic Scattering). [19]

CHAPTER 3

RADIATIVE TRANSFER MODELS

To obtain the colloids' response to the incident radiation, i.e., the spectral reflectance or transmittance of the colloids, the light transfer problem has to be solved. However, there is no general analytical solution to this problem, and hence there are many light transfer models based on restrictive assumptions. In this chapter we review the two most representative N-flux models, the Kubelka-Munk model and the four-flux model, to solve the light transfer problem. Moreover, we put forward a multilayer four-flux based Monte Carlo algorithm to study more general systems.

The study of light propagation in media that scatter and absorb light has developed an interest in many different disciplines such as astronomy [20, 21], atmospheric physics [22, 23, 24] and remote sensing [25, 26] among others. This study usually implies solving the radiative transfer equation (RTE) [27].

However, due to its complexity many resolution techniques and approximations have been suggested. A common approach is to use a N-flux model approximation to solve the RTE in systems with a plane-parallel geometry. N-flux models, firstly described in [28], separate light into N contributions each associated to an annular solid angle depending on its the angular distribution.[1] N can indeed be very large but models with low N present the advantage of providing simple formulae easily utilizable for macroscopic magnitudes, such as spectral transmission or reflectance. One well-known N-model is the Kubelka-Munk (KM) model [29]. The KM model consists of a two flux model in which light is split up into two isotropic diffuse fluxes propagating in the forward and backward directions. Despite its numerous applications, this model fails to provide accurate results under collimated incident illumination. To account for collimated contributions four-flux models, in which light is decomposed into two collimated and two diffuse components traveling in the forward and backward directions, were proposed.

Alongside analytical approximations, several numerical methods have been proposed. For example, a Monte Carlo (MC) approach using a multilayer four-flux model to describe the radiative transfer across multiple scattering media was presented in [30]. However, the MC inputs do not have a direct relationship with the media's properties. In this work, we introduce a MC approach based as well in a multilayer four-flux model in which the

[1] Despite these approximations, the largest source of error arises from neglecting the fact that light can be polarized.

probabilities of each layer are directly related to the system's physical properties.

In this chapter we review the aforementioned N-flux models, the KM model and the four-flux model, with special emphasis in the latter since we have utilized it to evaluate the spectral reflectance/transmittance in color computation. Furthermore, we put forward a multilayer four-flux MC algorithm that we have developed. This MC introduces new added capabilities such as temporal resolution (transient states) and spatial resolution (arbitrarily inhomogeneous media). This chapter is organized as follows: in section 3.1 we provide a brief overview of the KM model, while in section 3.2 a review of the four-flux model is provided. Finally, in section 3.3 we show the MC algorithm developed and an application of it to the study the temporal distribution of a δ-like pulse spread.

3.1 Kubelka-Munk model

The KM model, developed in 1931 in [29] to study paint films, is the most simple N-flux model used to study light transfer. Its most stringent restriction arises from the assumption of perfectly diffuse illumination. The system studied consists of a finitely thick plane-parallel scattering film placed on an arbitrary substrate which is shined on with completely diffuse light. A sketch of the system is given in fig. 3.1.

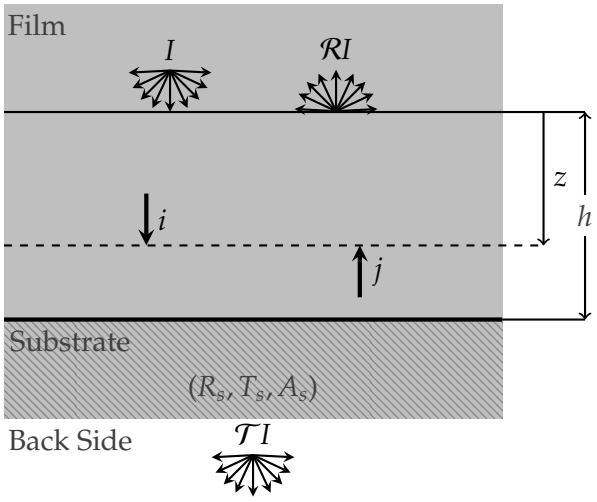

Figure 3.1: Sketch of the system and the fluxes. A finitely thick plane-parallel light-scattering medium (thickness $\equiv h$) placed in optical contact with an arbitrary substrate with know reflectance R_s, transmittance T_s and absorptance A_s.

Light transfer across the medium is modeled with two fluxes, a diffuse flux traveling toward positive z direction (i), and a diffuse flux traveling toward negative z direction (j). The fundamental equations of the KM model, based on energy balances, are the following:

$$\mathrm{d}i(z) = -(S+K)i(z)\,\mathrm{d}z + Sj(z)\,\mathrm{d}z \tag{3.1}$$

$$-\mathrm{d}j(z) = -(S+K)j(z)\,\mathrm{d}z + Sj(z)\,\mathrm{d}z\,, \tag{3.2}$$

where K and S are the absorption and back scattering coefficients. The solutions to eqs. (3.1) to (3.2) provided in [31] are

$$i(z) = I\frac{(a-R_s)\sinh bSz + b\cosh bSz}{(a-R_s)\sinh Sbh + b\cosh Sbh} \tag{3.3}$$

$$j(z) = I\frac{(1-aR_s)\sinh bSz + bR_s\cosh bSz}{(a-R_s)\sinh Sbh + b\cosh Sbh} \tag{3.4}$$

where $a = 1 + K/S$ is the albedo and $b = \sqrt{a^2 - 1}$. From the fluxes solution macroscopic magnitudes, such as the system's reflectance and transmittance, can be derived

$$R = \frac{(1 - aR_s)\sinh bSh + bR_s \cosh bSh}{(a - R_s)\sinh bSh + b\cosh bSh} \tag{3.5}$$

$$T = T_s \frac{b}{(a - R_s)\sinh bSh + b\cosh bSh} \tag{3.6}$$

3.2 Four-flux model

The four-flux model studies a system consisting of a parallel-planar medium, which embeds discrete homogeneous spherical particles, placed in optical contact with a substrate. The whole system is, in turn, stacked between two media, usually air. The scattering and absorbing properties of the medium can be derived from the Mie scattering theory, as proposed in [32]. Light propagation within the slab is modeled using the following fluxes:

(i) A collimated flux traveling toward positive z direction (I_c).

(ii) A collimated flux traveling toward negative z direction (J_c).

(iii) A diffuse flux traveling toward positive z direction (I_d).

(iv) A diffuse flux traveling toward negative z direction (J_d).

Figure 3.2 shows a sketch of the system and the fluxes considered.

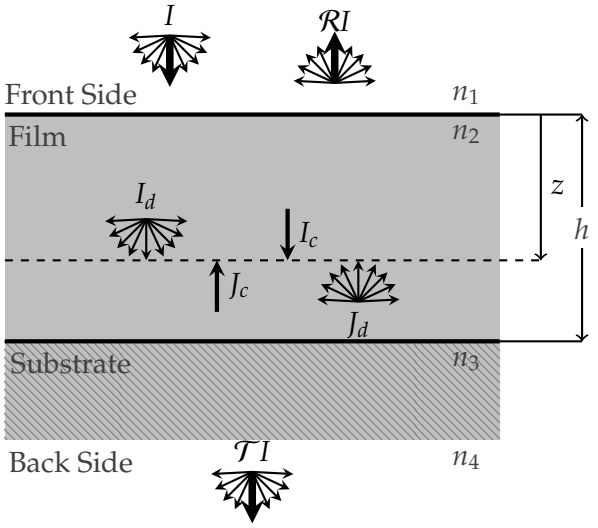

Figure 3.2: Sketch of the system and the fluxes. A finitely thick plane-parallel light-scattering medium (thickness ≡ h) placed in optical contact with an arbitrary substrate. The whole system is, in turn, stacked between two media, usually air ($n_1 = n_4 = 1$). n_i is the refractive index of the medium i. Light is partially collimated.

Taking into account the energy balances, the differential equations describing the system are

$$\frac{\mathrm{d}I_c}{\mathrm{d}z} = -(\alpha + \beta)I_c \tag{3.7}$$

$$\frac{\mathrm{d}J_c}{\mathrm{d}z} = (\alpha + \beta)J_c \tag{3.8}$$

$$\frac{\mathrm{d}I_d}{\mathrm{d}z} = \xi[(1 - \sigma_d)\alpha(J_d - I_d) - \beta I_d] + \sigma_c \alpha I_c + (1 - \sigma_c)\alpha J_c \tag{3.9}$$

$$\frac{\mathrm{d}J_d}{\mathrm{d}z} = \xi[\beta J_d + (1 - \sigma_d)\alpha(J_d - I_d)] - \sigma_c \alpha J_c - (1 - \sigma_c)\alpha I_c, \tag{3.10}$$

where α and β are the scattering and absorption coefficients per unit length, ξ is the average path length traveled by diffuse light as compared to collimated light, and σ_c and σ_d are the forward scattering ratio coefficients, i.e., the amount of light scattered into the forward hemisphere, for collimated and diffuse light respectively.[2,3] Note that in the case of diffuse light, the forward hemisphere relative to the film does not necessarily coincide with that relative to the beam.

In appendix C.1 we review thoroughly the four-flux model in the case of an infinite lateral slab with Mie scatterers embedded including an absorbing substrate, as a generalization of the revised version presented in [31] to any combination of collimated plus diffuse incidence. Special attention is paid to the case of absorptance, for which specific expressions are provided. Here, we simply show the solutions to eqs. (3.7) to (3.10)

$$I_c(z) = c_1 e^{-\zeta z} \tag{3.11}$$

$$J_c(z) = c_2 e^{\zeta z} \tag{3.12}$$

$$J_d(z) = c_3 \cosh(Az) + c_4 \sinh(Az) + c_5 e^{\zeta z} + c_6 e^{-\zeta z} \tag{3.13}$$

$$I_d(z) = c_7 \cosh(Az) + c_8 \sinh(Az) + c_9 e^{\zeta z} + c_{10} e^{-\zeta z}, \tag{3.14}$$

where only four coefficients, c_1, c_2, c_3 and c_4, are independent, and $\zeta = \alpha + \beta$ is the extinction coefficient per unit length. The expressions for the coefficients c_i and A are given in appendix C.1.

From eqs. (3.11) to (3.14), explicit expressions for the effective light transfer across the system can be obtained. The system's total reflectance and transmittance have a specular contribution ($\mathcal{R}_c$, $\mathcal{T}_c$), the light that has remained collimated, and a diffuse contribution composed of: i. the collimated incident light that is scattered ($\mathcal{R}_{cd}$, $\mathcal{T}_{cd}$), and ii. the diffuse incident light ($\mathcal{R}_{dd}$, $\mathcal{T}_{dd}$). Therefore, the total reflectance and transmittance can be expressed as

$$\mathcal{R} = f\mathcal{R}_c + \mathcal{R}_d = f(\mathcal{R}_c + \mathcal{R}_{cd}) + (1-f)\mathcal{R}_{dd} \tag{3.15}$$

$$\mathcal{T} = f\mathcal{T}_c + \mathcal{T}_d = f(\mathcal{T}_c + \mathcal{T}_{cd}) + (1-f)\mathcal{T}_{dd}, \tag{3.16}$$

where f is the fraction of collimated incident light. The specular and diffuse contributions to the total reflectance are

$$\mathcal{R}_c = r_{c12} + \frac{(1-r_{c12})^2 R_{sc} e^{-2\zeta h}}{1 - r_{c12} R_{sc} e^{-2\zeta h}} \tag{3.17}$$

$$\mathcal{R}_{cd} = \frac{(1-r_{d21})(1-r_{c12})e^{-\zeta h}[C_0 + C_1 e^{\zeta h} + C_2 e^{-\zeta h}]}{(A^2-\zeta^2)(1-r_{c12}R_{sc}e^{-2\zeta h})DEN} \tag{3.18}$$

$$\mathcal{R}_{dd} = r_{d12} - \frac{(1-r_{d21})(1-r_{d12})}{DEN} \times [AR_{sd}\cosh(Ah) + (E - R_{sd}D)\sinh(Ah)], \tag{3.19}$$

[2]Parameters involved in the four-flux model are studied in more detail in appendix C.2.

[3]α (eq. (C.50)) and β (eq. (C.51)), and σ_c (eq. (C.52)) and σ_d (eq. (C.53)) are directly related to the scattering and absorption cross sections, and the phase functions of LPRs respectively.

and the contributions to the transmittance are

$$\mathcal{T}_c = \frac{(1-r_{c23})(1-r_{c34})\tau_c(1-r_{c12})\mathrm{e}^{-\zeta h}}{(1-r_{c23}r_{c34}\tau_c^2)(1-r_{c12}R_{sc}\mathrm{e}^{-2\zeta h})} \tag{3.20}$$

$$\begin{aligned}\mathcal{T}_{cd} = &\left[(1-r_{c12})(1-r_{d23})(1-r_{d34})\tau_d\mathrm{e}^{-\zeta h}\right] \\ &\times \frac{D_1\cosh(Ah)+D_2\sinh(Ah)+D_3\mathrm{e}^{\zeta h}+D_4\mathrm{e}^{-\zeta h}}{(1-r_{d32}r_{d34}\tau_d^2)(1-r_{c12}R_{sc}\mathrm{e}^{-\zeta h})(A^2-\zeta^2)DEN}\end{aligned} \tag{3.21}$$

$$\mathcal{T}_{dd} = -\frac{(1-r_{d12})(1-r_{d23})(1-r_{d34})A\tau_d}{(1-r_{d32}r_{d34}\tau_d^2)DEN}, \tag{3.22}$$

where r_{cij} and r_{dij} are the reflectance factors[4] for collimated and diffuse light[5] at the interface between media i and j, DEN is given by

$$\begin{aligned}DEN = &A(R_{sd}r_{d21}-1)\cosh(Ah) \\ &+[E(R_{sd}+r_{d21})-D(1+r_{d21}R_{sd})]\sinh(Ah),\end{aligned} \tag{3.23}$$

coefficients C_i and D_i as well as the effective reflection coefficients for collimated and diffuse radiation at the film-substrate interface R_{sc} and R_{sd} are given in appendix C.1.

If the incident light is completely diffuse ($f = 0$) and only the film and the substrate are considered, the KM equations are recovered.

This analytical model is used to evaluate either the reflectance or transmittance spectrum of the metallic NPs colloids, essential in the color coordinates computations.

3.3 Multilayer Four-flux Monte Carlo

In order to simulate the four-flux theoretical model, we implement a MC approach. Specifically, we discretize the film in N layers and couple it to additional layers that account for: reflections at the different interfaces (air-film, film-substrate, substrate and substrate-air), and the absorption at the substrate. We assign absorption, reflection and scattering probabilities to each layer (including the substrate).

Table 3.1 shows the correspondence between the different probabilities considered in our MC approach and the physical parameters of the four-flux theory.

Figure 3.3 shows the probability *allocation* for diffuse and collimated beams, respectively. We send N_T elemental light beams to the specimen and decide their fate according to the algorithm given in appendix C.3.

The MC simulation model outputs the total number of reflected, transmitted and absorbed beams, the total number of beams hitting a given layer (associated to the transverse energy density $\mathcal{U}(z)$) and the total number of time units [6] of each beam before being either reflected, transmitted or absorbed, which may be associated to its time-of-flight (ToF).

[4] Expressions for evaluating the reflectance factors from media's refractive indices are given in appendix C.2.
[5] The factors greatly depend upon whether the diffuse flux is incident toward positive or negative z.
[6] Let a time unit be the time that a collimated beam takes to cross of a layer of the vacuum, i.e., $n = 1$.

Probability	Physical parameter	Description
PK^{col}	$\beta\,\mathrm{d}z$	Absorption probability for a collimated beam
PK^{dif}	$\xi\beta\,\mathrm{d}z$	Absorption probability for a diffuse beam
PR^{col}	r_{cij}	(Fresnel) Reflection probability for a collimated beam
PR^{dif}	r_{dij}	(Fresnel) Reflection probability for a diffuse beam
$PS^{\text{col}}_{\text{back}}$	$\alpha(1-\sigma_c)\,\mathrm{d}z$	Backscattering probability for a collimated beam
$PS^{\text{dif}}_{\text{back}}$	$\xi\alpha(1-\sigma_d)\,\mathrm{d}z$	Backscattering probability for a diffuse beam
$PS^{\text{col}}_{\text{forward}}$	$\alpha\sigma_c\,\mathrm{d}z$	Forward scattering probability for a collimated beam

Table 3.1: Correspondence between the different probabilities considered in our MC approach and the physical parameters of the four-flux theory.

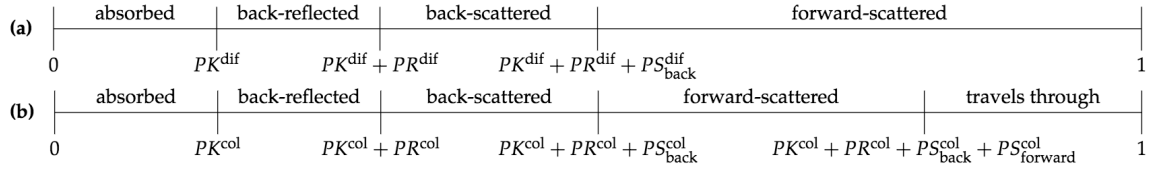

Figure 3.3: Probability *allocation* for: **(a)** a diffuse beam and **(b)** a collimated beam.

As it will be shown, the total number of incoming beams, N_T, determines the precision of the calculation, or the statistical uncertainty, i.e., the difference between consecutive realizations under the same simulation conditions. On the other hand, the accuracy of the calculation, i.e., the difference between the real and the simulated values, depends on the total number of layers, N. Given that the total probability for a beam to be scattered (absorbed) within the medium αh (βh) must be equal to the product of N times the layers' probability for scattering (absorption), N can be defined as

$$N = \frac{(\xi+1)\zeta h - \xi\alpha\sigma_d h}{\sum_i P_i}\,, \tag{3.24}$$

where

$$\sum_i P_i = PK^{\text{col}} + PK^{\text{dif}} + PS^{\text{col}}_{\text{back}} + PS^{\text{dif}}_{\text{back}} + PS^{\text{col}}_{\text{forward}}\,. \tag{3.25}$$

It should be noted that the total event probability for a collimated (diffuse) photon is only $PK^{\text{col}} + PS^{\text{col}}_{\text{back}} + PS^{\text{col}}_{\text{forward}}$ ($PK^{\text{dif}} + PS^{\text{dif}}_{\text{back}}$) which is always $\leq \sum_i P_i$. Therefore the criterion given in eq. (3.25) is even more restrictive. The total event probability for each layer, $\sum_i P_i$, directly determines the number of layers needed to correctly describe the physical phenomena taking place, and reproduce the theoretical results. Apart from the obvious probability limit $\sum_i P_i \leq 1$, a convergence criterion must be established. As our MC model implements the same assumptions as the four-flux model described before, for a first verification we compare simulated and theoretical results of the collimated and diffuse reflectance, $\mathcal{R}_c$ and $\mathcal{R}_d$, and transmittance, $\mathcal{T}_c$ and $\mathcal{T}_d$. Figure 3.4 shows the difference (in percentage points) between simulated and theoretical results of $\mathcal{T}_c$ as a function of the number of layers and $\sum_i P_i$. Similar results are obtained for the other magnitudes.

As can be seen in fig. 3.4, for $\sum_i P_i = 0.01$ the absolute difference between simulated and exact results is already stabilized, so that we take

$$\sum_i P_i \leq 0.01 \tag{3.26}$$

as a discretization criterion. As a means to visualize the effect of the discretization in a typical case, we set $\alpha = 0.5$ mm^{-1}, $\beta = 0.05$ mm^{-1}, $h = 1$ mm, $n_1 = n_4 = 1.0$, $n_2 = 1.5$, $n_3 = 1.0$, $\sigma_c = 0.5$, $\sigma_d = 0.5$, $\xi = 2$, $\tau_c = 1$, $\tau_d = \tau_c^2$, $f = 1.0$ and calculate $\mathcal{R}_c$, $\mathcal{R}_d$, $\mathcal{T}_c$ and $\mathcal{T}_d$ for several levels of discretization (growing N_T, progressively lower $\sum_i P_i$), as a function of ζh, the net extinction within the medium. For each discretization, 100 realizations were carried out, calculating an average value together with the associated standard deviation.

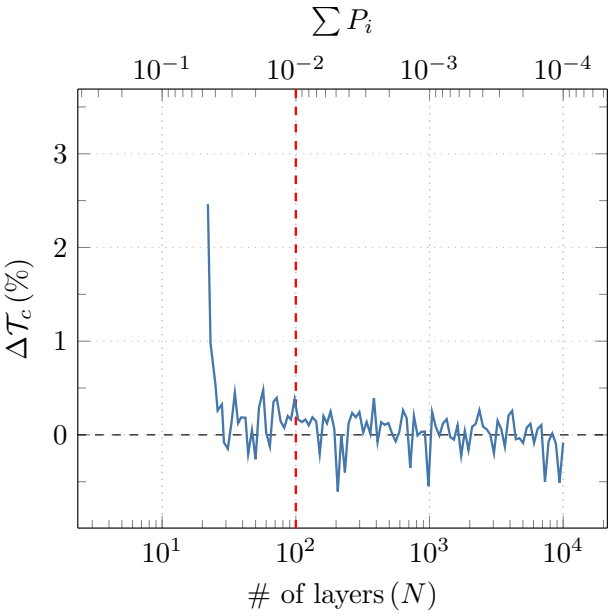

Figure 3.4: Absolute difference (in percentage points) between simulated and theoretical results of the collimated transmittance, as a function of N and $\sum_i P_i$ (top axis). Parameters: $\alpha = 0.4$ mm^{-1}, $\beta = (1 - 2\alpha)/3$ mm^{-1}, $h = 1$ mm, $n_1 = n_3 = n_4 = 1.0$, $n_2 = 1.8$, $\tau_c = 1$, $f = 0.5$.

Table 3.2 shows average values ± standard deviation of the differences (in percentage points) between simulated and theoretical results of $\mathcal{R}_c$, $\mathcal{R}_d$, $\mathcal{T}_c$ and $\mathcal{T}_d$ as a function of ζh. As expected, simulated results converge (with an excellent agreement) to theoretical ones as N_T is increased and $\sum_i P_i$ is decreased, i.e., discretization layers are made thinner for the same specimen. Interestingly, as $\sum_i P_i$ decreases we achieve more accuracy (average value approaches zero) while increasing N_T reduces the overall noise associated with the random number generation.

N_T	$\sum_i P_i$	$\langle\Delta\mathcal{R}_c\rangle$ (%)	$\langle\Delta\mathcal{R}_d\rangle$ (%)	$\langle\Delta\mathcal{T}_c\rangle$ (%)	$\langle\Delta\mathcal{T}_d\rangle$ (%)
50	0.5	-6 ± 12	6 ± 6	-9 ± 18	-18 ± 36
10^3	0.1	0 ± 2	0.9 ± 0.7	-2 ± 3	-3 ± 4
10^5	0.01	0.0 ± 0.2	0.09 ± 0.07	-0.2 ± 0.5	-0.5 ± 1.0

Table 3.2: Average values ± standard deviation of $\mathcal{R}_c$, $\mathcal{R}_d$, $\mathcal{T}_c$ and $\mathcal{T}_d$ differences (in percentage points) between simulated and theoretical results along ζh, for several combinations of N_T and $\sum_i P_i$.

3.3.1 Time-of-Flight (ToF)

MC also tracks the ToF of each beam, i.e., the number of time units elapsed by each beam before it is either reflected, transmitted or absorbed. This magnitude provides useful information that it is not available analytically, e.g., the temporal distribution of a pulse of light or, equivalently, the transient state of the magnitudes $\mathcal{R}_c$, $\mathcal{T}_c$, etc.

As an illustrative example we have studied the temporal distribution of an ultra-short collimated pulse incident on a heterogeneous system composed of two layers of different translucent media over a substrate, see fig. 3.5. The layer closest to the substrate has a larger scattering and absorption contribution than the other. This system can represent the case of a sequence of two different coatings applied to a transparent substrate. The system of layers is embedded in air. The pulse can be modeled as a $\delta(t = 0)$ by sending a bunch of N_T beams at a specific time.

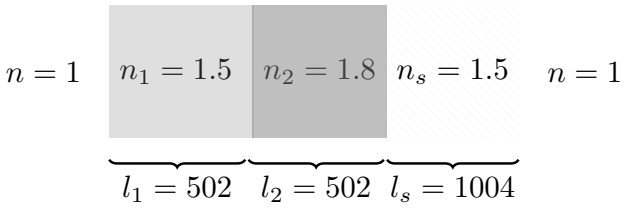

Figure 3.5: Sketch of the system under study. The media's parameters (α[mm^{-1}],β[mm^{-1}],h[mm]) are given below. Medium 1: (0.1,0.1,1), medium 2: (1,1,1), substrate (0,0,2). l_i correspond to the number of layers in which the media has been discretized.

Let the time that a collimated beam takes to cross a layer of a medium with refractive index $n = 1$, i.e., in vacuum, be a time element Δt. Under uniform discretization, the time elapsed by a collimated (diffuse) beam to go through a layer with refractive index n is $t_c = n\Delta t$ ($t_d = \xi n\Delta t$). The temporal distribution of a collimated pulse incident on the system is shown in fig. 3.6.

For a delta function-like pulse, the collimated magnitudes take non-zero values at specific times while the diffuse magnitudes are spread over time. This is a result of collimated beams traveling all together as a ballistic bunch, being susceptible of exiting the system only when it reaches the system's edges. The perturbation within the system due to the pulse decreases as beams are either reflected, transmitted or absorbed. Thus, we observe in fig. 3.6 that the (%) of beams decreases with increasing time.

Let us analyze each magnitude individually. Regarding the collimated reflectance (blue bars in fig. 3.6, top), the first peak ($t = 0$) corresponds to light that is reflected at the first interface. The second contribution ($t = 2n_1l_1 \simeq 1506$) is due to light that crosses the first medium, suffers a reflection at the interface between the media and exits the system from the first interface. The third ($t = 4n_1l_1 \simeq 3013$) comes from the small amount of beams that suffers several reflections at the following interfaces: medium 1-medium 2, medium 1-air and medium 1-medium 2. The fourth peak ($t = 2(n_1l_1 + n_2l_2) \simeq 3317$) arises due to light that is reflected at the medium 2-substrate interface. The following peaks can be understood using similar arguments. Analogously, if we analyze the collimated transmittance's peaks (orange bars in fig. 3.6, top) we see that the first one ($t = n_1l_1+n_2l_2+n_sl_s \simeq 3163$) corresponds to light that crosses the whole system and goes through the last interface. The second peak is light that reflects at the interface medium 1-medium 2, reflects back at the interface air-medium 1 and leaves the system from the back side ($t = 2n_1l_1 + n_2l_2 + n_sl_s \simeq 4669$), etc.

In the case of diffuse reflectance we can see a continuous contribution from light that enters the system, suffers multiple scattering eventually turning around exiting the system at the first interface. We also observe periodical enhancements. The enhancements occur

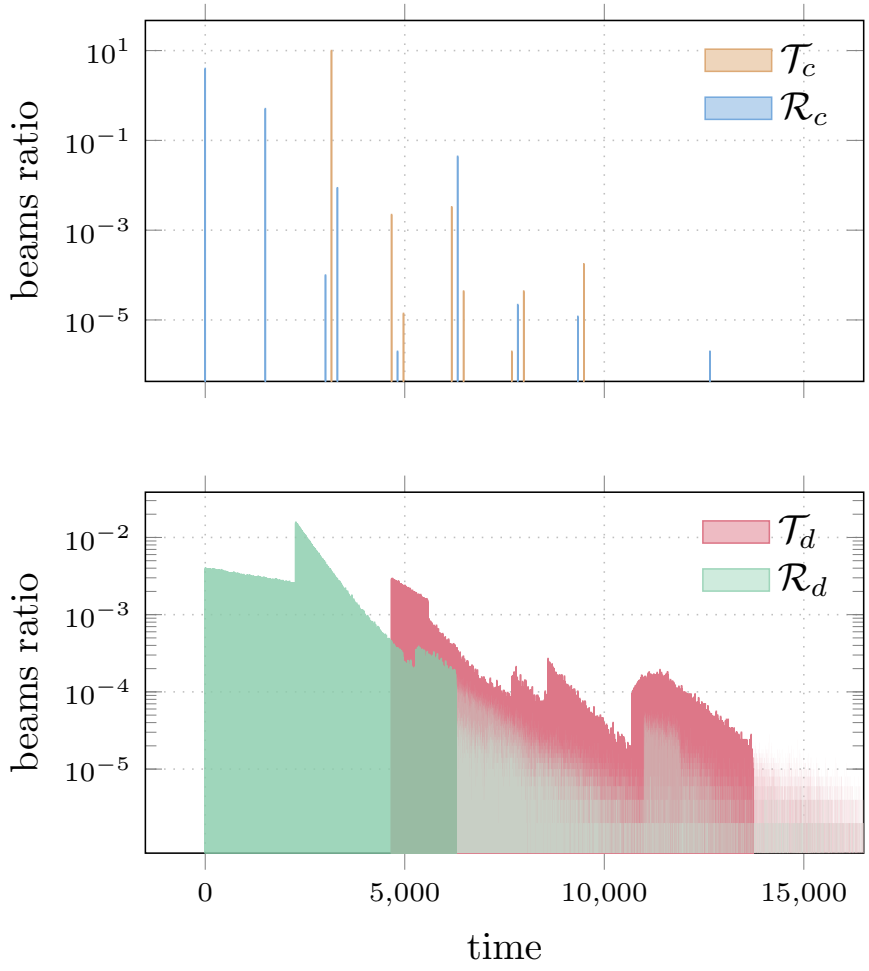

Figure 3.6: Response function of the system to a delta-like pulse. Histogram showing the ratio of collimated and diffuse beams that have been either reflected or transmitted as a function of time. The bin width is equal to a time element Δt. The total number of incident beams utilized in this simulation is: $N_T = 5 \times 10^7$.

when the ballistic bunch reaches the first interface. New diffuse beams coming from the scattering of the collimated bunch add to the continuous background of diffuse beams yielding an increase in the diffuse reflectance. With regard to the diffuse transmittance, it starts at $t = n_1 l_1 + n_2(l_2 - 1) + 2(n_2 + n_s l_s) \simeq 4670$, i.e., light that has remained collimated until experiencing scattering at the end of the medium 2 layer. It behaves like the diffuse reflectance with the exception that the enhancements occur when the ballistic bunch arrives at the last interface.

Note that all collimated transmitted pulses but the first one, will be overlapped with the transmitted diffuse contribution since they have similar intensities. On the other hand, there are several collimated reflected pulses with a significantly larger intensity than the reflected diffuse contribution even at time over $6000\Delta t$.

Figure 3.6 shows the system's impulse-response function. Therefore, the system's response to a pulse described by a general function of time ($f \equiv f(t)$) is simply the convolution of the pulse's function and the system's impulse-response function.

CHAPTER 4

COLOR SCIENCE

The aim of this chapter is to examine the most important concepts of color science which will be applied to metallic NPs colloids in the subsequent chapter. There are three aspects involved in color perception: the observed object, the illuminant and the observer. Tools to obtain the spectral response of metallic NPs colloids have been given in the previous two chapters. This chapter covers the other aspects left in color calculation, i.e., the illuminant and the observer. Moreover, it shows insightful ways to represent color as well as means equations to compute color differences.

Contrary to popular belief, color is not an inherent property of objects but a human sensation, i.e., the feeling or perception produced after the brain has processed a physical stimulus, in this case the spectral electromagnetic power collected at the retina. The psycophysical nature of color prevents it from being accessed by scientific measurements. What can be measured is the stimulus that yields the color perception. Colorimetry is the field devoted to the study and metric of the physical stimuli responsible for this visual sensation.

There are three aspects which determine the physical stimulus: the light source's spectral power density (SPD), scattering and absorbing properties of media located along the light path and the observer's color matching functions (CMFs), i.e., the eyes' spectral response.

The aim of this chapter is to review briefly the underlying physics behind color science and provide the means necessary to evaluate color coordinates and represent them in an intuitive way. The chapter is organized as follows: in section 4.1 the fundamental concepts of colorimetry are outlined; section 4.2 provides the equations to evaluate trichromatic color coordinates and the CIE's SPDs of standard illuminants and CMFs of standard observers; in section 4.3 we look over the most popular color spaces used in color representation; and, lastly, section 4.4 briefly explains how to calculate differences between pairs of colors.

4.1 Fundamentals of Colorimetry

First of all, we review the basic concepts under which colorimetry is built on. In section 4.1.1, we describe briefly how the physical stimuli that yield color sensation occur, and in section 4.1.2 we present the empirical laws on which the colorimetry is built.

4.1.1 Color perception

As previously stated, color perception is produced by the brain processing the light detected in eye. Thus, the physical stimulus depends on: (i) the SPD of the light entering the detector, i.e., the human eyes, and (ii) the human vision.

(i) Light that reaches the eyes can come either directly from a light source or, either reflected or transmitted from an object. In the former case, the SPD of light collected in the eyes is simply the source's SPD while, in the later, the source's SPD experiences a change as light interacts with the object via absorption, scattering, etc. In either case there will be no visual image unless at least part of the SPD overlaps part of the visible spectrum, whose wavelengths go from 380-780 nm approximately.

(ii) The human vision mechanism can be split into two stages. A first stage where the luminous signal is detected in the eyes, and a second stage in which the signal is sent to brain where, ultimately, it is analyzed. In the first one, light entering through the pupil is focused onto the retina by the eye's lens. It is in the retina where the specialized cells responsible for light perception, rods and cones, reside. While rods are specialized in scotopic or night vision, i.e., vision at low levels of illumination, and enable us to distinguish shapes through a gray scale, cones respond primarily at photopic levels of illumination, i.e., high levels of illumination, and are responsible for color perception. There are three types of cones whose sensitivity peaks in different parts of the spectrum, which can be split up into red, green and blue even though sensitivities spectra overlap. When light hits those cells a chemical response is triggered. This response is responsible for creating an electrical impulse directed to the brain where the signal is eventually processed.

Due to the trichromatic nature of color vision, a color can be understood in a 3-D space, i.e., it can be identified as a linear combination of three chromatic coordinates:

$$\mathbf{C} = c_1\mathbf{x}_1 + c_2\mathbf{x}_2 + c_3\mathbf{x}_3 \tag{4.1}$$

where $\mathbf{x}_i$ are the unitary stimuli of a particular trichromatic system and c_i the weights which can be evaluated from the following expression

$$c_i = \int_{\lambda_1}^{\lambda_2} \bar{x}_i(\lambda) P(\lambda) d\lambda \tag{4.2}$$

where $\bar{x}_i(\lambda)$ is one of the color matching functions (CMFs), i.e., the amount of each unitary stimulus needed to match every monochromatic element of the equi-energy spectrum[1]; $P(\lambda)$ is the SPD of the light incident on the eye[2]; and λ_1 and λ_2 the wavelengths that limit the visible spectrum.

[1] An equi-energy spectrum is any spectrum whose spectral concentration of a radiometric quantity is constant throughout the visible region.

[2] The SPD can be either the SPD of a source if we are observing a source directly or the product of a source's SPD, and either the spectral reflectance or transmittance of the object under observation.

4.1.2 Colorimetry Basic Laws

The brain process involved in color perception rules out the possibility of building an analytical theory, with our current brain understanding, and hence the modern colorimetry basis relies on empirical laws. These laws are built on additive color mixing (lights with wavelengths lying on different spectral ranges are added) as they are simpler than those for subtractive color mixing (when part of the light spectrum is removed). Additive color mixing satisfy the following rules [33]

1. At least three independent variables are required to specify a color match.
2. Only the tristimulus values are relevant, not their spectral compositions. [3]
3. A gradual change of one or more components of a color mixture leads to a gradual change in the resulting tristimulus values.

CIE colorimetry, which is the world-reference color theory, is based on and is consistent with these laws.

4.2 Commission Internationale de l'Éclairage. CIE Standards

The CIE is an international scientific technical non-profit organization focused on the international cooperation and exchange of information related to light, illumination, color, and color spaces. It was the pioneer in defining a Standard Observer for Colorimetry in 1931. A standard that still remains valid, although there have been updates (CIE 1964 standard observer). Moreover, not only it provides standards for the observers, but also it provides SPDs of standard illuminants with a widespread use in many industrial fields, such as the paint industry [29] or printing applications [34].

In this section we show the CMFs of both the 1931 and the 1964 CIE Standard Observer as well as the SPDs of the most common standard illuminants.

4.2.1 CIE Standard Illuminants

The CIE has standardized the SPDs of ordinary light sources, e.g., a tungsten lightbulb, the daylight light, etc., in order to provide a standard in control or colorimetric characterizations measurements. Specifically, as only the relative SPDs are required in color calculations, they provide SPDs of theoretical sources, called illuminants. [4] Physical implementations of these theoretical sources are the so-called CIE sources.

Among all possible light sources, the CIE has introduced illuminants that represent: a typical incandescent light (illuminant A); the direct sunlight (illuminant B), currently obsolete; average daylight (illuminants C and D[5]); and an equienergy, i.e., wavelength independt, SPD (illuminant E) . Figure 4.1 shows the relative SPDs of some common illuminants.

We observe from fig. 4.1 that, unlike the rest, the illuminant A spectral shape is very

[3] This results in the phenomenon of metamerism, i.e., unequal physical characteristics (different SPDs) can lead to colors that are considered equivalent.

[4] The SPD are normalized relative to the value at $\lambda = 530$ nm.

[5] The latter are more up to date.

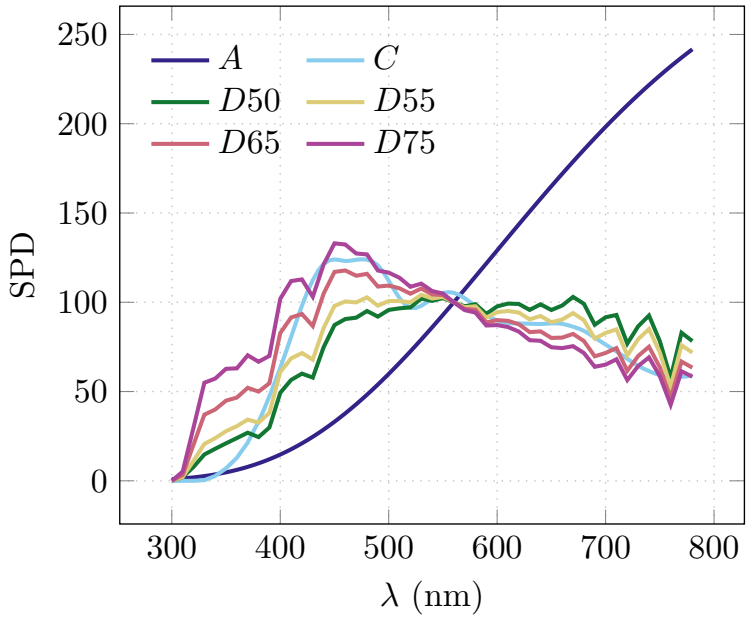

Figure 4.1: Relative SPDs of several CIE standards illuminants.

smooth and indeed can be expressed with a mathematical function. This happens as the SPD is well approximated to the spectral radiation of a black body with a temperature of approximate T = 2856 K.

Daylight is the most natural form of illumination for human-beings but it depends on several factors. Some of these factors are the weather conditions, the time of the day, the season of the year, etc. Therefore, the CIE has put forward several D illuminants which describe diverse phases of daylight. CIE recommends the use of D65 which represents the average daylight. [6]

The illuminant C is not as popular since it is only defined in the visible spectrum and is slightly purplish compared to some phases of daylight.

4.2.2 CIE Standard Observers

A standard observer is characterized by a set of CMFs obtained under some given observation conditions. CIE introduced two different standard observers, one in 1931 and the other in 1964. The experiments for both observers were performed with a dark surrounding but with different foveal fields of observation. The former used 2° foveal field while the latter used a 10°. The CIE recommendation is to use generally the second observer as the CIE 1931 observer is only well suited for small stimuli (~ 1-4° angular size).

The idea behind the experiments carried out to establish the CMFs of a observer is simple. An observer is shown a color that has to be matched with the help of three primaries, a red, a green and a blue light. The relative amount of a primary used is the corresponding weight for that primary. The experiment is carried out for a wide range of spectral colors under

[6] We have used the D65 illuminant SPD in the color calculations.

some observations conditions for a sufficiently large sample of observers. In in fig. 4.2a the results for the 1931 observer are shown.

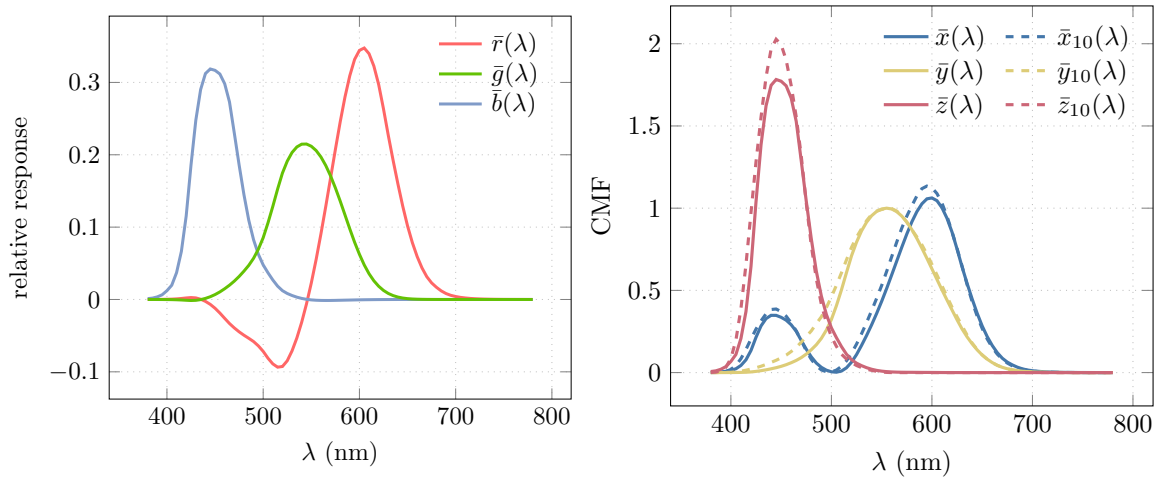

(a) RGB CMFs

(b) xyz CMFs

Figure 4.2: CIE's RGB CMFs of the 1931 observer and CIE's xyz CMFs of the 1931 (solid lines) and 1964 (dashed lines) spectral observers.

Back then, when computers were not available, the negative lobes present in the RGB CMFs complicated significantly color evaluations. Negative values appear when a given primary had to be added to the target color instead to the rest of the primaries. Thus, the CIE substituted the red, green, and blue primaries for some new mathematical primaries in order to remove the negative lobes. The imaginary primaries are called tristimulus values and can be obtained from the RGB values by matrix transformation, see appendix D.1. The CMFs of the tristimulus values can be obtained using the same conversion. The CMFs of the both CIE observers are shown in fig. 4.2b. The $\bar{y}$ CMF has the particularity of matching the luminous-efficiency of the eye, i.e., the average spectral sensitivity of human visual perception of brightness.

The tristimulus values can be evaluated from the spectral information of the illuminant, observer and object using the following expressions

$$X = F \int_{\lambda_1}^{\lambda_2} P(\lambda)\bar{x}(\lambda)\,\mathrm{d}\lambda \quad (4.3) \qquad Y = F \int_{\lambda_1}^{\lambda_2} P(\lambda)\bar{y}(\lambda)\,\mathrm{d}\lambda \quad (4.4) \qquad Z = F \int_{\lambda_1}^{\lambda_2} P(\lambda)\bar{z}(\lambda)\,\mathrm{d}\lambda \quad (4.5)$$

where $\bar{x}(\lambda)$, $\bar{y}(\lambda)$, and $\bar{z}(\lambda)$ are the CMFs of either the 1931 or the 1964 CIE observer[7], $P(\lambda) = \phi(\lambda)S(\lambda)$ where $S(\lambda)$ is the source's SPD and $\phi(\lambda)$ is either the reflectance or the transmittance spectrum, and F is a normalization value defined by

$$F = \frac{100}{\int_{\lambda_1}^{\lambda_2} S(\lambda).y(\lambda)\,\mathrm{d}\lambda}. \quad (4.6)$$

[7]We have used the xyz CMFs of the 1964 CIE standard observer in the color calculations.

4.3 Color Representation. Color Spaces

There exists many color representations, a.k.a., color spaces. Some color spaces might be more suitable than others depending on the application of color. In this section we present some of the most representative color spaces. [8]

4.3.1 RGB Color Space

A RGB color space is any color space that results from adding red, green and blue light together in diverse ways to reproduce a wide range of colors. A specific RGB color space is characterized by the three trichromatic coordinates, the red, green, and blue additive primaries, as well as a white point, and a gamma correction curve.[9]

RGB color spaces are the most widespread color spaces in computer graphics due to their simplicity. The most popular color spaces are the sRGB and Adobe RGB which has a significantly larger gamut[10], see fig. 4.3. The most significant disadvantages of RGB color spaces are that they are not device independent and that does not cover the whole human gamut. In the following chapter, the colors shown on the plots are the actual colors calculated. To display them on the screen we have used the sRGB coordinates. Therefore, despite our attempts to display the genuine colors of metallic NPs colloids, some of the most saturated colors were impossible to be simulated on a screen.

4.3.2 XYZ Color Space and Chromaticity Diagram

The XYZ color space is the standard color space developed by the CIE. It is based on three mathematical primaries know as the tristimulus units XYZ. Unlike for RGB color spaces, all the colors perceivable by the human eye are contained in the XYZ color space.

Generally, color is represented in the 2-dimensional CIE chromaticity diagram xy rather than in a 3-dimensional space which is less insightful. An example of the chromaticity diagram is shown in fig. 4.3. The x and y coordinates are two of the chromaticity values defined as

$$x = \frac{X}{X+Y+Z} \qquad y = \frac{Y}{X+Y+Z} \qquad z = \frac{Z}{X+Y+Z} \tag{4.7}$$

which are not independent $z = 1 - x - y$. To completely characterize a color an additional variable, usually the luminance Y, is required.

Although it contains the whole human gamut, this color space has some disadvantages. First, the coordinates have no clear relation with physical characteristics of colors. Moreover, similar variations of the chromaticity values can lead to very different changes in color perception, i.e., an equal difference in the values can result in the color perceived be extremely different or barely indistinguishable.

[8] In appendix D.1 equations to convert chromatic coordinates among different color spaces are given.

[9] The gamma correction curve is a non-linear operation used to encode or decode the luminance of either image or video systems as their response are commonly non-linear.

[10] The human gamut consists of all the colors that are perceivable by the human eye.

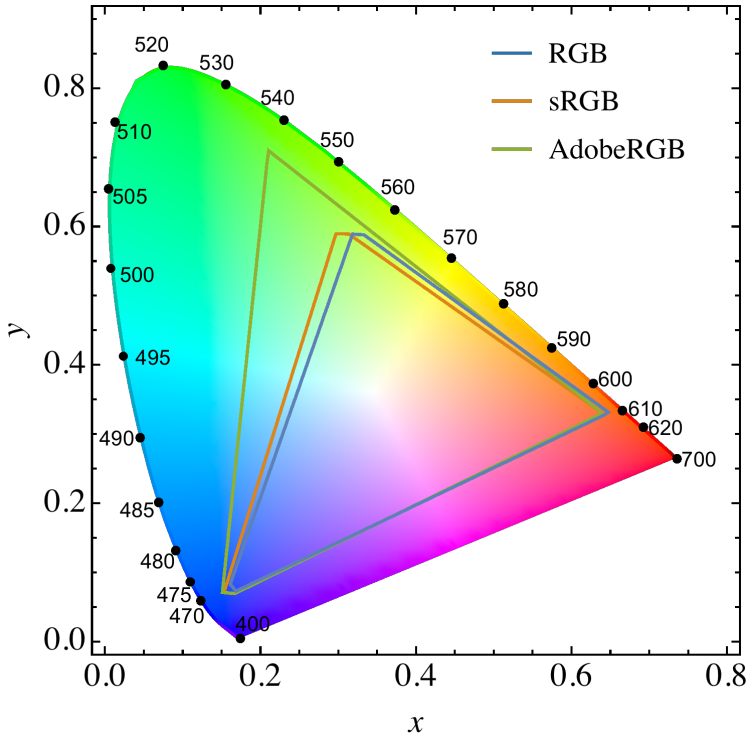

Figure 4.3: xyY Chromaticity diagram with the RGB, sRGB and AdobeRGB gamuts shown. The colors at the edge are the primary colors, i.e., the spectral colors.

4.3.3 CIELAB and CIELCh Color Space

The CIELAB and CIELCH are color spaces that, like the XYZ color space, can describe all human perceivable colors. The CIELAB color space was introduced as a form of color representation whose magnitudes are linearly proportional to color perception, i.e., a given change in the color value yields an equivalently proportional change in color perception.

The CIELAB coordinates are the brightness (L^*), with the extreme values being $L^* = 0$ (black) and $L^* = 100$ (white), the position between green and red colors (a^*), where more negative values represent greener colors and more positive values redder, and the position between blue and yellow colors (b^*), where more negative values represent bluer colors and more positive values more yellow. Commonly, colors are represented in the ab plane, i.e., the plane resulting from cutting the color space at given L^*, as in fig. 4.4.

Despite the advantages with respect to the XYZ space, besides the brightness, the CIELAB magnitudes are not intuitive, and thus the CIELCH color space was proposed. Color coordinates in CIELCH space are easily obtained from CIELAB coordinates and share the majority of the advantages of the CIELAB coordinates. Moreover, unlike in the CIELAB space, each coordinate has a physical meaning.

The L^* coordinate is equivalent to the brightness in the CIELAB space. Lower values are related to darker colors while larger values to lighter colors. The C^* coordinate is called chroma or "saturation". It provides an idea of colors purity. A primary or spectral color is "pure" and has a large chroma value, while mixed colors have lower values. White, grey

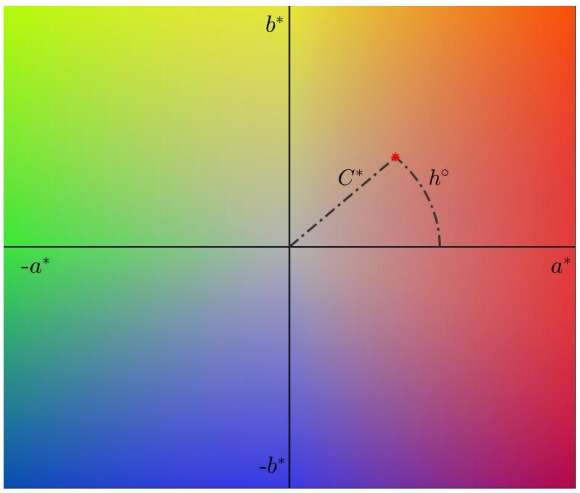

Figure 4.4: Color representation on the ab plane with the chroma and hue highlighted.

and black colors are obtained using an equal amount of primaries (with different concentrations). Thus, they are totally unsaturated and have a null chroma value. The h° coordinate is known as hue. It is represented in the ab plane as angle and gives information about the type of color, e.g, values closer to 0° lead to red colors, angles near 90° yellow, around 180° green, and about 270° blue, see fig. 4.4.

4.4 CIE Color Differences

The ability of reproducing the color of specific products is of vital importance to the industry. CIE colorimetry allow us to test quantitatively the color differences between a pair of specimens. Fortunately for the industry, our eyes are not as sensitive as the optical devices. There is a threshold over which colors are perceivably different and indistinguishable otherwise. [11] To compare two colors, we only require a magnitude proportional to the visual difference between two colors. If the value is smaller than the perceivable threshold the colors are said to be equivalent.

CIE proposed to define color differences as distances in the color spaces. However, there is an unavoidable matter known as the "perceptual uniformity" that has to be addressed. The distance between a color and a reference is "perceptual uniform" if, the color is contained in the color subspace composed of all the points that are at a distance smaller than the perceivable threshold from the reference color. These distances should be independent of the color reference. This independence has not been always guarantied and the CIE has refined the distance definition over the years to overcome this problem. Currently, the most updated and widely used formula is the CIEDE00, ΔE_{00}, given in appendix D.2. [12]

[11] Studies have shown that for values $\Delta E^*_{ab} \lesssim 2.3$, where ΔE^*_{ab} is the euclidean distance between the color coordinates of two colors in the CIELab, are not noticeable by the human eye [35]. This upper limit is also known as the just noticeable distance (JND).

[12] There have not been studies on the JND for the color differences ΔE_{00}. However, color authorities have stated that the JND may be approximately around $\Delta E_{00} \sim 1.5$.

CHAPTER 5

COLOR OF METALLIC NANOPARTICLES

Finally, we are able to evaluate the chromatic coordinates of metallic NPs colloids. The LPRs characteristics, which are responsible for the color of the aforementioned, depend strongly on the optical properties of the metallic NPs, their size, their shape, and the embedding medium, among other factors. Thus, in this chapter, the relation between the trichromatic LCh coordinates and those aspects is studied.

The focus of previous chapters was principally on providing the means necessary to conduct color calculations. Therefore, in this chapter we finally address the principal objective of this project, the study of the color dependence on the properties of metallic NPs colloids.

A colloid is defined as "a solid, liquid, or gaseous substance made up of very small, insoluble particles (as single large molecules or masses of smaller molecules) that remain in suspension in a surrounding solid, liquid, or gaseous medium of different matter" [1]. Thus, a colloid can be for example gold NPs dispersed in an aqueous medium, a stained glass, etc. In the following we have assumed that the metallic NPs colloids are free-standing, i.e., the colloids are suspended in air. Thus, the refractive indices of the four-flux model n_1, n_3, and n_4 are equal to unity (the refractive index of air), and $n_2 \equiv n_{sm}$.

This chapter is structured in four sections each of them covering a crucial aspect in the LPRs characteristics determination, and hence in color. The sections are the following: section 5.1 where the color of colloids is studied as a function of the NPs optical properties; section 5.2 where the dependence on size is analyzed; in section 5.3 we show how color varies as the refractive of the embedding medium does, and finally section 5.4 studies color as a function of spheroidal NPs' aspect ratios.

5.1 Nanoparticles Optical Properties

As mentioned before, the effect of LPRs was not understood until the beginning of the 20th century with Mie's scattering theory. However, empirical applications of LPRs, e.g., glass coloring, date back to ancient times with the Lycurgus cup (400 AC) being one of the most classical examples. In the Middle Ages, the stained glass manufacturing sector flourished [36] since the variety of metallic NPs utilized skyrocketed . An example of colorful magnificent stained glass windows is the rose window ("el Rosetón") at the León Cathedral,

located in north-wester Spain.

In chapter 2 we saw that the resonant frequency depended heavily on the optical properties of the metallic NPs. Colloids with different metallic NPs inclusions show completely different colors. For example, we see in fig. 2.1 that the absorption efficiency of spherical silver colloids presents an enhancement around the bluish wavelengths while TiN NPs colloids show it at higher wavelengths (from green to red wavelengths). Therefore there is little blue (green-orange) light transmitted across Ag (TiN) colloids. In other words, the transmitted color of Ag (TiN) colloids looks orangish (bluish). We have studied the color in transmission of several stained glasses with similar concentrations of various spherical metallic NPs. The results are shown in fig. 5.1.

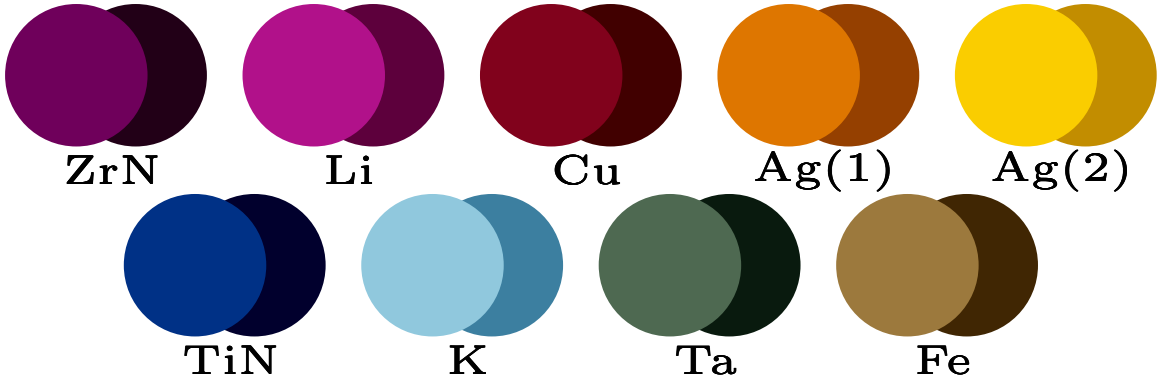

Figure 5.1: Stained glass color palette. Transmitted color of diverse stained glasses made of glass ($n_{sm} = 1.5$) and inclusions of the metallic NPs shown. The colors in the foreground (background) are obtained when the incident light is totally collimated $f = 1$ (diffuse $f = 0$), the colloids' width is $h = 1$cm, and the NPs radius is $r = 25$ nm. The colors displayed are genuine.

The results are shown for both totally collimated and diffuse light to analyze the difference between the opposite illuminations. The color difference ΔE_{00} is given in table 5.1. Moreover, table 5.1 provides the concentrations as well as the mean inter-particle distance $\langle r \rangle$ for each element, where $\langle r \rangle$ is defined as

$$\langle r \rangle = \left(\frac{3}{4\pi\rho_n} \right)^{1/3} . \tag{5.1}$$

where ρ_n is the particle number density. We see from table 5.1 that all the mean interpar-

Element	ZrN	Li	Cu	Ag (1)	Ag (2)	TiN	K	Ta	Fe
ρ_n (mm^{-3})	$5.9{\cdot}10^7$	$2.1{\cdot}10^7$	$7.3{\cdot}10^7$	$8.4{\cdot}10^7$	$2.1{\cdot}10^7$	$8.4{\cdot}10^7$	$8.4{\cdot}10^7$	$10{\cdot}10^7$	$8.4{\cdot}10^7$
$\langle r \rangle$ (nm)	1600	2200	1500	1400	2200	1400	1400	1300	1400
ΔE_{00}	19.6	19.4	14.0	24.4	17.4	17.6	23.0	25.8	29.5

Table 5.1: Metallic NPs concentrations, mean interparticle distances and color difference between collimated and diffuse illumination.

ticle distances are significantly larger than the NPs size and therefore the assumption of negligible NPs interactions done in the Mie theory holds.

Also different number particle densities ρ_n lead to pretty different colors as we can see if we compare Ag(1) with Ag(2). An increase in ρ_n implies more light-NPs interactions, and thus more absorbed light. The transmitted colors of colloids with larger ρ_n look darker. This effect is also achieved if we increase the width of the colloid h [37]. However, if ρ_n is too large, $\langle r \rangle$ will no longer be larger than the NPs size and interaction effects will become relevant.

The color differences between the color under collimated or diffuse light are substantially large and are indeed appreciated by the human eye, see section 4.4. The illumination is another important factor in color perception and should not be taken for granted (specially at a clothing store).

5.1.1 Lycurgus cup

The Lycurgus cup has been found to have metallic nano-inclusions, mostly of a silver and gold alloy with a ratio silver to gold 7:3 [38]. Although the silver and gold NPs might interact creating alloys, we have tried to reproduce the Lycurgus reflected/transmitted colors with a simple model. We have assumed that the silver and gold NPs neither aggregate nor interact. We have evaluated the color transmitted and reflected by spherical silver (gold) colloids within a glass embedding (n_{sm} = 1.5) with radii between 10-100 nm.

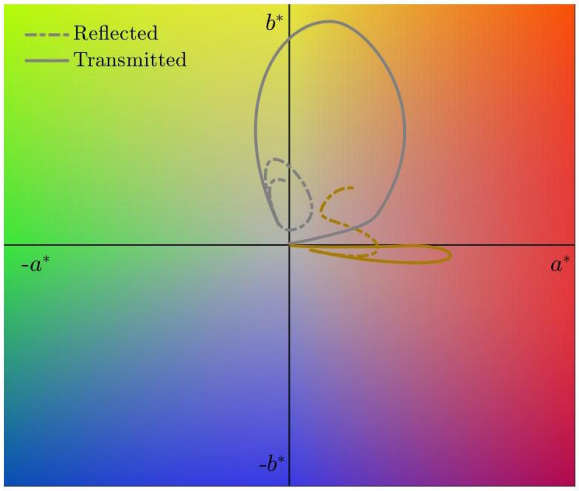

Figure 5.2: Color trajectories on the ab plane of silver (gray lines) and gold colloids (golden lines) with varying radii, n_{sm} = 1.5.

Figure 5.2 shows the trajectories on the ab plane of the transmitted/reflected color as the size changes. The LCh trichromatic coordinates of those trajectories are shown in fig. 5.3.

We observe that the color of the light reflected by silver inclusions goes through the green color region. Indeed, we see in fig. 5.3 that for small radii the reflected color of silver NPs is light green. The reflected color of gold colloids does not reach the greens. Human vision is more sensitive to green colors, see $\bar{y}$ in fig. 4.2b, hence we can infer that the reflected green color arises from light interaction with the silver NPs.

In the case of transmittance, both the silver and the gold NPs produce colors on the red quadrant. Therefore, the red color obtained in transmission can be obtained by a combination of both.

5.2 Nanoparticles Size

The size of the metallic NPs is crucial in the determination of the resonant frequency of the LPRs and so is in determining the color of metallic colloids. Here we study the color dependence with the radius of spherical metallic NPs colloids, in particular Au and Ag NPs. The trichromatic coordinates of stained glasses with either Au or Ag spherical inclusions as a function of the radius are shown in fig. 5.3.

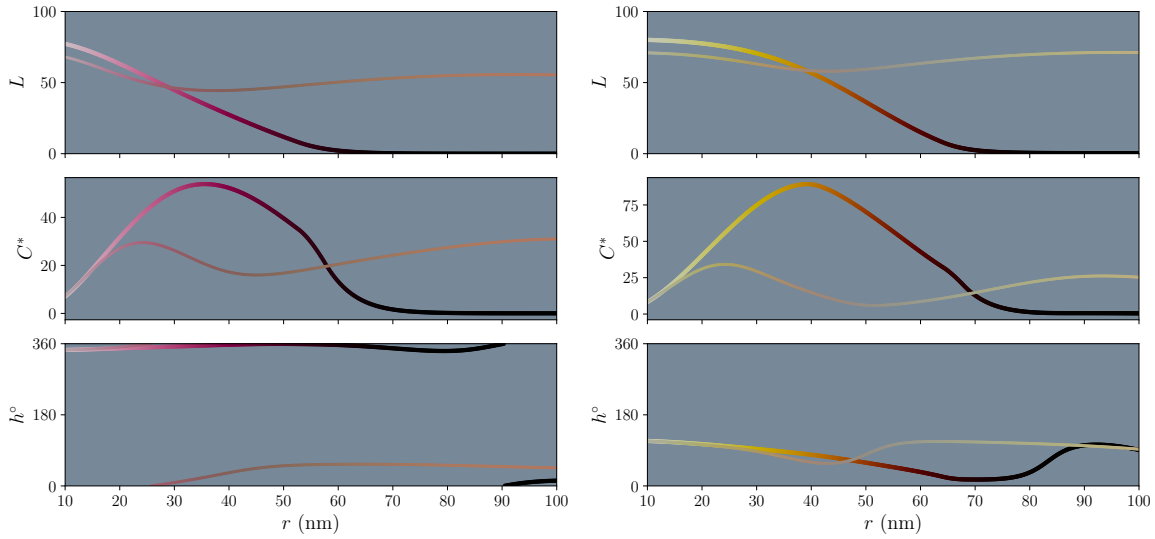

(a) Gold NPs (b) Silver NPs

Figure 5.3: Trichromatic LCh coordinates of the color of spherical metallic NPs colloids as a function of their radii. The embedding medium refractive index is $n_{sm} = 1.5$, the concentration of the NPs inclusions is $\rho_n = 10^7$ mm^3, the width of the system is $h = 1$ cm, and the incident radiation is completely diffuse ($f = 0$). The lines' color is genuine. The thick (thin) line corresponds to the transmitted (reflected) color.

The results are similar for both metals, hence let us analyze the behavior of color coordinates of the gold colloid based on the results shown in fig. 2.2. In the case of transmitted light we observe that the brightness decreases with increasing the radius. This is a consequence of two effects: i. the absorption efficiency grows with increasing radii, and ii. as the size of the radii increases, the probability for light interacting with an inclusion rises. Therefore, the light absorbed within the colloid increase monotonically as the radii grows until all is absorbed, i.e., no light is transmitted (black color). On the other hand, reflected light is a mixture of light reflected at the first interface air-colloid and light that has been scattered back. Therefore, the larger the scattering efficiency the higher the likelihood of light being reflected. At low radii the absorption efficiency grows faster than the scattering efficiency which results in a smooth decay of the brightness since part of the light previously reflected is now absorbed. However, if the size is further increased the scattering efficiency becomes larger and more light is reflected yielding an increase of L^*. The brightness reaches a plateau when the amount of light absorbed becomes maximum.

With regard to the chroma, at low radii it takes low values since the absorption and scattering efficiencies are low, i.e., only a small fraction of the incident radiation is absorbed

or scattered, and hence the light reflected/transmitted is almost the incident light's color, i.e., the D65 illuminant's color, approximately white. The transmitted chroma shows a maximum since there are competitive effects. An increase in the radii results in an increment of the absorption efficiency near the resonant frequency which results in a smaller contribution of those wavelengths in the transmittance spectrum. The less uniformly distributed the spectrum is, the purer the color which results in larger chroma values. However, as the radii increases less light is transmitted, and the transmitted color darkens until is completely black, i.e., null chroma. In the case of the reflected light the chroma behavior depends on the relative amount of light scattering vs. absorbed. First, at lower radii the absorption is larger than the scattering at frequencies near the resonance. Therefore, there is a smaller contribution to the reflectance spectrum at those frequencies and the reflected color becomes "purer". We also observe (in the hue) that, at those sizes, the color reflected and transmitted is very similar. However, at larger radii scattering is more important than absorption and the contribution at those frequencies grows. As a result, the chroma decreases and the reflected light turns to a color different from the transmitted one. With increasing scattering, the contribution to the reflected light of the scattered frequencies rises yielding an increment of the chroma. It is worth noting that the increment of the chroma in the first place came as a decrease in the contribution of some parts of the spectrum, and the second from an increase of some part of the spectrum. This is the reason why the reflected color shows significantly different hues at different radii, pink at lower radii and orangish at larger.

We saw in fig. 2.2 that for radii < 50 nm both the scattering and absorption efficiencies experience a red-shift with increasing radius. This results in a slight variation of the hue of both transmitted and reflected light. For larger radii, the spectral efficiencies flatten and the hue becomes approximately constant.

5.2.1 Size distribution

As mentioned in chapter 1 there are many modern synthesis processes able to produce monodisperse NPs with custom properties. In particular, the seeded growth technique allows generating NPs with uniform quasi-spherical shape as well as a narrow distribution for radius up to ~200 nm [39], or even ~300 nm [40]. However, the size distribution of the NPs is not symmetrical, it is usually skewed toward larger radii [41].

To study the effect on color of the size distribution we have applied a weighting function to the radius-dependent spectral reflectance $R(r, \lambda)$ or transmittance $T(r, \lambda)$. Then, we have evaluated the color coordinates from the resulting spectral reflectance or transmittance and computed the color difference between the color from the weighted spectral reflectance or transmittance and the unweighted. The weighted spectrum is obtained using

$$\bar{\phi}(\lambda) = \frac{\int_a^b w(r)\phi(r,\lambda)dr}{\int_a^b \phi(r,\lambda)dr}, \tag{5.2}$$

where $w(r)$ is the weighting function. We have used the skew-normal distribution as $w(r)$ to take into account the asymmetry in the distribution

$$w(r) = \frac{2}{\omega}\psi\left(\frac{x - x_o}{\omega}\right)\Psi\left(\gamma\left(\frac{x - x_o}{\omega}\right)\right), \tag{5.3}$$

where x_o and ω are the location and scale parameters, $\psi(x)$ and $\Psi(x)$ are the normal distribution function and its cumulative function respectively,

$$\psi(x) = \frac{1}{\sqrt{2\pi}}\exp\left(-\frac{1}{2}(x)^2\right), \qquad \Psi(x) = \frac{1}{2}\left(1 + \text{erf}\left(\frac{x}{\sqrt{2}}\right)\right), \tag{5.4}$$

and γ is a parameter related to the skewness of the distribution. If $\gamma > 0$ ($\gamma < 0$) the distribution is right (left) skewed. The results are shown in fig. 5.4.

Figure 5.4 shows the color difference between NPs with a δ-like size distribution, and with skew-gaussian size distribution for two different values of γ. In the latter, the standard deviation has been fixed to 2 nm, a value compatible with experimental results [40], [39]. The solid (dashed) lines show the difference of the colors in transmission (reflection) color. The difference is larger at small radii than at large radii. This may occur since the relative standard deviation is larger at small radii. The color differences between the δ-like and the skew-gaussian size distribution are related to the spatial derivatives of the trichromatic coordinates. If the weight of a radius r_* with $\partial x_i/\partial r|_{r_*} \gg$, where x_i is one of the color coordinates, is non-negligible for a skew-gaussian distribution and negligible for a δ-like distribution ($\delta(r - r_0)$), i.e., $r_* \neq r_0$, the color difference will be large.

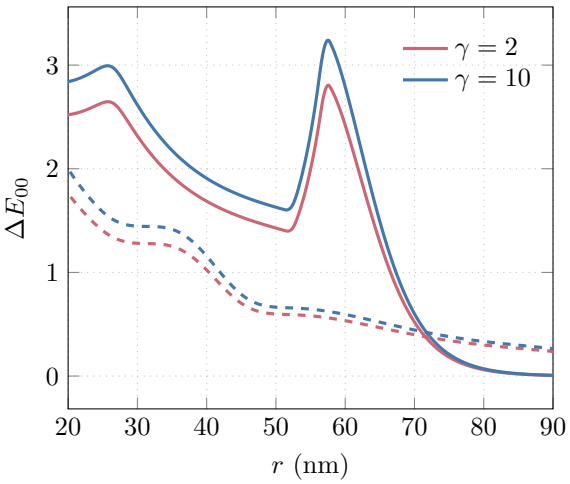

Figure 5.4: ΔE_{00} color difference between the color of gold colloids when the size distribution is considered and when not. Solid (dashed) lines corresponds to transmitted (reflected) colors.

In the case of transmission we observe two peaks which can be explained from the chroma behavior shown in fig. 5.3. The color difference grows at small radii until radii close to the chroma maximum ($\partial C^*/\partial r \sim 0$) become relevant in the skew-gaussian average, and the color difference starts decreasing. It follows that trend until around $r \sim 50$ nm where the sharp slope change at $r \sim 55$ nm contributes significantly to the average. The difference is null at very large radii since no light is transmitted.

Regarding to the reflected color, the color difference decays progressively more steeply around $r \sim$ 20-30 nm when the brightness variation is larger and at $r \sim 40$ nm when there is a larger hue variation. The color difference is almost zero at larger radii as the reflected color tends to a saturation value.

5.3 Dielectric Environment

Another relevant factor that influences the color of metallic colloids is the optical constants of the surrounding medium. To study this effect we have evaluated the trichromatic coordinates of the transmitted color of spherical gold and silver colloids as a function of the refractive index of the embedding medium. The results are displayed in fig. 5.5.

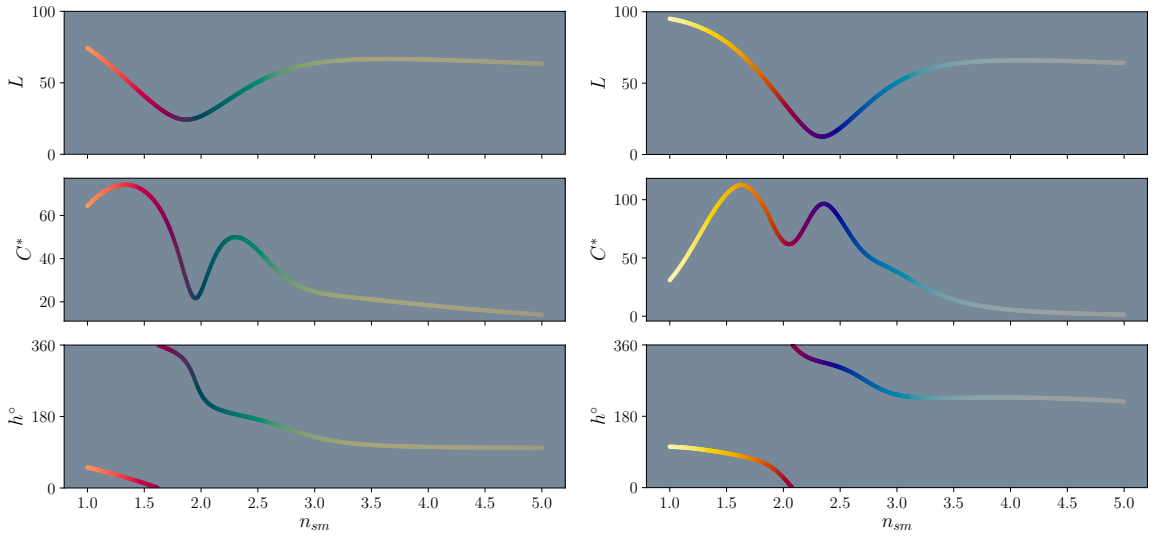

(a) Gold NPs (b) Silver NPs

Figure 5.5: Trichromatic LCh coordinates of the transmitted color of spherical metallic NPs colloids as a function of the refractive index of the surrounding medium. The embedding NPs radius is $r = 25$ nm, the concentration of the NPs inclusions is $\rho_n = 10^8$ mm^3, the width of the system is $h = 1$ cm, and the incident radiation is totally collimated ($f = 1$). The color shown is genuine.

We notice from fig. 5.5 that the embedding medium plays a major role in the color of metallic colloids. The most distinctive feature of fig. 5.5 is the large hue variations with n_{sm}. The colors are very saturated since the incident radiation is completely collimated.

These massive hue variations can be explained using the results of the spectral absorption efficiencies dependence on n_{sm} fig. 2.4. Here we focus on the case of silver colloids. Similar arguments apply to gold colloids. At low refractive indices, the transmitted light has a major contribution at wavelengths ranging from approximately 580 to 780 nm, where Q_{abs} is very low. Since humans are more sensitive to colors at the center of the spectrum, see $\bar{y}$ in fig. 4.2b, the color perceived is more yellow than red. As n_{sm} increases the resonant wavelength is red-shifted and the colors becomes redder. This also results in an increase of the chroma since fewer wavelengths are mixed. At $n_{sm} \sim 2.3$ the contributions from the bluest and the reddest part of the visible spectrum are similar and the final color perceived is purple. This mixture reduces the "purity" of the transmitted color, and we observe a decrease of the chroma. As the LPRs are more red-shifted the contribution from the red side lessens leading to another chroma rise. In this regime the colloid shows a navy tone that turns into cyan as the greener light contribution grows (with a consequent chroma decay). For large n_{sm} the resonant frequency is no longer in the visible spectrum. There is

no preferred wavelength and the final color is gray, i.e., almost null chroma values.

The brightness depends heavily on the amount of total absorbed light. For example, it is very large at either low or high values of n_{sm} when the total absorption within the colloid is not significant. Moreover, it shows a minimum when the total absorption is maximum that is approximate at $n_{sm} \sim 2.4$, when the resonant frequency is close to the human brightness sensitivity peak.

5.4 Nanoparticles Shape. Spheroids

Both the spectral characteristics of LPRs and color are very sensitive to the shape of NPs. In this section, we have studied the transmitted color dependence on the aspect ratio of gold spheroids. The results are displayed in fig. 5.6.

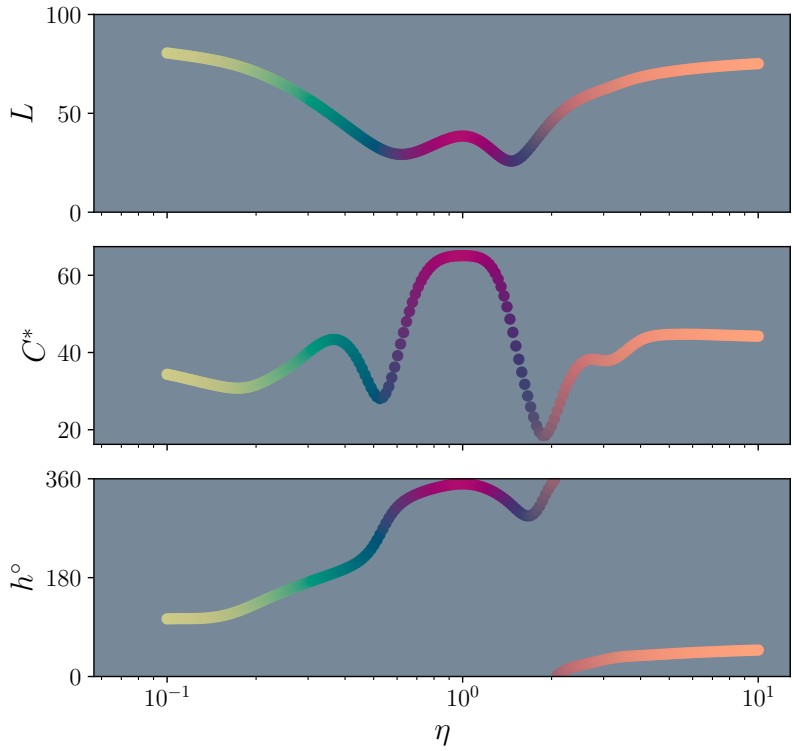

Figure 5.6: Trichromatic LCh coordinates of the transmitted color of spheroidal gold colloids as a function of the aspect ratio defined in section 2.2.4. The volume equivalent radius is $r_V = 25$ nm, the particle number density is $\rho_n = 10^7$ mm^3, the width of the system is $h = 1$ cm, the refractive index of the embedding medium is $n_{sm} = 1.5$, and the incident radiation is unpolarized totally collimated ($f = 1$). The color shown is genuine.

We infer from fig. 5.6 that small deviations from the spherical shape do not lead to significant changes in the color. However, dramatic changes are observed when the shape departs considerably from this ideal shape.

From fig. 2.6 we infer that under unpolarized light, the oblate response is similar to a sphere with radius a. Thus, the effect of decreasing η is similar to that of increasing the size.

The explanation for the hue and the chroma is similar to the one presented in section 5.3. As the LPRs moves towards larger λ values the contribution from the blue and the red part of the spectrum becomes comparable and the colloid shows a purplish tone. A further red-shift results in diminishing the reddest contribution and the colloid turns blue. When the contribution from wavelengths around the mid-part of the spectrum grows, the color starts looking greener due to the human largest sensibility at those wavelengths. Unlike the silver colloids, when the resonant frequency is out of the visible spectrum the gold colloids look yellowish instead of white/gray due to interband transitions.

The case of prolate spheroids is a bit more complex. The absorption cross section of a prolate spheroid is similar to the response of two spheres one with radius a and the other with radius c. For a given r_V, the a and c semi-axes follow a power-law relation with η with exponents $-1/3$ and $2/3$ respectively, eqs. (2.4) and (2.5). Therefore, color changes arise mainly from variations on LPRs properties of the equivalent sphere with radius c. As η increases the LPRs of the sphere with radius a move slightly towards shorter wavelengths but remains in the mid-part of the spectrum. That is why green colors do not appear in gold prolate spheroids. An increase in η results in an increment of c and similar arguments as for the oblate case apply. When the resonant frequency is not longer in the visible part the colloid shows an orangish color since the blue and green part of the spectrum is removed by interband transitions and interactions with effective smaller sphere.

CHAPTER 6

SUMMARY AND FUTURE OUTLOOK

This closing chapter summarizes the main results obtained in this work and discusses prospective applications of: i. the color dependence on metallic NPs colloids properties, ii. the four-flux model and numerical implementations of it, and iii. metallic NPs.

Recapping, in chapter 1 we provided a background on metallic NPs and their relationship with color. Chapter 2, chapter 3 and chapter 4 were devoted to the study of the fundamental aspects involved in color calculations. In chapter 5 we finally performed a systematic study of the color of metallic NPs colloids. And, lastly, in this chapter we highlight the most relevant results of the previous chapters.

Although the primary objective was to study the relationship between the color of metallic NPs colloids and their plasmonic properties, we have researched other related topics, e.g., transport models. Thus, in this chapter we point out some possible applications not only of the colorimetric properties of metallic NPs colloids, but also of the rest of the subjects covered.

This chapter is divided in two sections. In the first one, section 6.1, we sum up and highlight the most relevant results, while in the other, section 6.2, we propose several potential applications of the present work.

6.1 Summary

In the past few decades, a lot of attention has been placed on metallic NPs due to their vast applicability in a wide range of fields such as biomedicine, communications, environmental sciences, etc. All those applications rely on the enhancement of the electric field in the NPs surroundings, a phenomenon known as LPRs. A distinctive consequence of this phenomenon is the astonishing color properties that some metallic NPs colloids show. Color is an intricate magnitude and its evalution is not straight-forward. Therefore, we studied first how to calculate the color of metallic NPs colloids, and then analyzed its dependence on LPRs characteristics.

First, we have studied the LPRs' spectral behavior dependence on metallic NPs colloids properties, specifically the NPs optical properties, size, shape, and the embedding medium. We have observed that both the resonant frequencies and the spectral shapes of LPRs depend greatly on the optical properties of NPs. We have distinguished two regimes regarding

the size of the NPs; a small regime where only the dipolar mode is excited, and a large regime where multipolar contributions and collective effects appear. Moreover, we have observed that the angular distribution of the scattered field depends on the relative size between the NPs size and the incident λ, i.e., x. When $x \ll 1$ the scattered field is almost isotropic, while for large x it is predominantly scattered in the forward direction. We have also noticed that an increase of the embedding medium's refractive index yields a red-shift of the resonant frequency. If n_{sm} is sufficiently large the resonant frequency is no longer in the visible spectrum. Finally, we have studied the spectral behavior of LPRs varying the aspect ratio of spheroids, under both linearly polarized and unpolarized light. We have seen that under linearly polarized light, the LPRs generated are equivalent to those created by spherical NPs with radii equal to the spheroid's semilength along the direction of polarization. Since, spheroids have two different semi-axis lengths LPRs show two peaks when illuminating with unpolarized light.

In order to be able to obtain macroscopic magnitudes, such as the spectral reflectance of transmittance of an object, we have studied radiative transport models. In particular, we focused on two N-flux models, i.e., models where infinite lateral extension is assumed, the KM model and the four-flux model. Moreover, we have introduced a MC approach based on a multilayer four-flux model which shows some advantages with respect to analytical models. For example, it allows the study of transient states as well as arbitrarily inhomogeneous media. We have used the analytical four-flux model in combination with the MC to: i. set a discretization criterion for the MC, and ii. validate its convergence. To show the capabilities of the MC we have obtained the response of a layered heterogeneous medium to a δ-like pulse of light. The system's response to a more general light pulse described by a function of time $f(t)$ can be obtained from the convolution of $f(t)$ and the system's response to a δ-like pulse.

We have reviewed the basis of color science. We described the mechanism of color perception in which three aspects are involved: the object, the illuminant and the observer. In addition, we provided SPDs of standard illuminants and the CMFs of standard observers. Besides, we showed different ways of representing color coordinates in an insightful way. Lastly, we provided standardized formulae to calculate color differences between pairs of colors.

Finally, we analyzed the color of metallic NPs colloids dependence on the NPs optical properties, NPs size, NPs shape and the optical properties of the embedding medium. We have studied the color of different NPs embedded in glass ($n_{sm} = 1.5$) and simulated a "color palette" of stained glasses. Furthermore, we have reproduced the colors of the Lycurgus cup assuming non-interacting independent silver and gold inclusions. Additionally, we surveyed the color dependence on the NPs size for both Ag and Au NPs; and analyzed the applicability of the assumption of a δ-like size distribution by computing the color differences between this case and the case where the size distribution resembles more the experimental size distribution. We saw that larger errors were commited at smaller radii. We have noticed as well that there is a large hue variation when the refractive index of the embedding medium changes. We have concluded that it is a result of a red-shift of the resonant frequency of LPRs with increasing n_{sm}. This effect would be difficult to observe experimentally since common solvents do not have large refractive indices, usually

$n_{sm} \in (1, 2)$. Finally, we investigated the relationship between the color and the aspect ratio of gold NPs colloids. We observed that in the case of oblate (prolate) spheroids the color is similar to the color of colloids with spherical inclusions with $r \simeq a$ ($r \simeq c$). The semiaxis length a (c) is inversely (directly) proportional to η. Therefore, an increase in η in oblate (prolate) spheroids yields results equivalent to decreasing (increasing) r in the case of perfect sphericity.

6.2 Prospective Applications

Some potential applications have been cataloged according to the topic of the study.

Color of Metallic Nanoparticles Colloids

The initial idea of this work was to establish an empirical relationship between the size of metallic NPs and their color. This relation could have been potentially used in the development of an alternative approach to conventional methods for characterizing NPs colloids with the advantage of being more economical and faster. However, the relation is not simple and is not bijective. Moreover, this method could not provide information relative to the size distribution.

However, industries where coloring techniques are applied, such as the glass industry, can benefit from this study. For example, coloring glasses with the use of metallic NPs has some advantages with respect to other ways of coloring, e.g., coloring with pigments. For example, the color of metallic NPs colloids does not fade away since it is a result of light interacting with the inclusions. Moreover, stained glasses are no longer restricted to cathedrals and can be used to decorate furniture, as the main element in modern art pieces, etc.

This study could be enriched in a future with an experimental validation of the results shown in chapter 5.

Four-flux model and Monte-Carlo

Both analytical and numerical radiative transfer model have applications on wide range of fields such as astronomy, atmospheric physics, remote sensing. In particular, the MC tool that we have introduced can be used in the paint industry as it allows for the calculation of light transfer in heterogeneous media such as a stack of different paint layers and coatings.

It is worth noting that these models are applicable to other type of radiations, such as thermal radiation which broadens the applicability spectrum of these tools.

Optimal LPRs

Every application of metallic NPs has an optimal performance when the LPRs satisfy some specific properties. A lot of efforts are being made by the scientific community in the search of the optimal NPs [15]. Knowing how different parameters affect the LPRs eases the search.

BIBLIOGRAPHY

[1] Collins Dictionaries. *Collins english dictionary*. HarperCollins Publishers, 2009.

[2] Eleonora Petryayeva and Ulrich J Krull. Localized surface plasmon resonance: nanostructures, bioassays and biosensing—a review. *Analytica chimica acta*, 706(1):8–24, 2011.

[3] Miguel A García. Surface plasmons in metallic nanoparticles: fundamentals and applications. *Journal of Physics D: Applied Physics*, 44(28):283001, 2011.

[4] Stefan A Maier and Harry A Atwater. Plasmonics: Localization and guiding of electromagnetic energy in metal/dielectric structures. *Journal of applied physics*, 98(1):10, 2005.

[5] Katherine A Willets and Richard P Van Duyne. Localized surface plasmon resonance spectroscopy and sensing. *Annu. Rev. Phys. Chem.*, 58:267–297, 2007.

[6] Umair Yaqub Qazi and Rahat Javaid. A review on metal nanostructures: Preparation methods and their potential applications. *Advances in Nanoparticles*, 5(01):27, 2016.

[7] S Anu Mary Ealia and MP Saravanakumar. A review on the classification, characterisation, synthesis of nanoparticles and their application. In *IOP Conference Series: Materials Science and Engineering*, volume 263, page 032019. IOP Publishing, 2017.

[8] Wenbo Hou and Stephen B Cronin. A review of surface plasmon resonance-enhanced photocatalysis. *Advanced Functional Materials*, 23(13):1612–1619, 2013.

[9] Katrin Kneipp, Yang Wang, Harald Kneipp, Lev T Perelman, Irving Itzkan, Ramachandra R Dasari, and Michael S Feld. Single molecule detection using surface-enhanced raman scattering (sers). *Physical review letters*, 78(9):1667, 1997.

[10] Martin A Green. Prospects for photovoltaic efficiency enhancement using low-dimensional structures. *Nanotechnology*, 11(4):401, 2000.

[11] PJ McNulty, HW Chew, and M Kerker. Inelastic light scattering. In *Aerosol Microphysics I*, pages 89–116. Springer, 1980.

[12] Craig F Bohren and Donald R Huffman. *Absorption and scattering by a sphere*. Wiley Online Library, 1983.

[13] Gustav Mie. Beiträge zur optik trüber medien, speziell kolloidaler metallösungen. *Annalen der physik*, 330(3):377–445, 1908.

[14] Thomas Wriedt et al. A review of elastic light scattering theories. *Particle & particle systems characterization*, 15(2):67–74, 1998.

[15] Adrien Lalisse, Gilles Tessier, Jérome Plain, and Guillaume Baffou. Quantifying the efficiency of plasmonic materials for near-field enhancement and photothermal conversion. *The Journal of Physical Chemistry C*, 119(45):25518–25528, 2015.

[16] Gelon Albrecht, Monika Ubl, Stefan Kaiser, Harald Giessen, and Mario Hentschel. Comprehensive study of plasmonic materials in the visible and near-infrared: linear, refractory, and nonlinear optical properties. *ACS Photonics*, 5(3):1058–1067, 2018.

[17] Sadao Adachi. *The Handbook on Optical Constants of Metals: In Tables and Figures*. World Scientific, 2012.

[18] Donald R Huffman. The applicability of bulk optical constants to small particles. In *Optical Effects Associated with Small Particles*, pages 277–324. World Scientific, 1988.

[19] WRC Somerville, B Auguié, and EC Le Ru. Smarties: user-friendly codes for fast and accurate calculations of light scattering by spheroids. *Journal of Quantitative Spectroscopy and Radiative Transfer*, 174:39–55, 2016.

[20] Arthur Schuster. Radiation through a foggy atmosphere. *The astrophysical journal*, 21:1, 1905.

[21] Yichen Zhang and Jonathan C Tan. Radiation transfer of models of massive star formation. i. dependence on basic core properties. *The Astrophysical Journal*, 733(1):55, 2011.

[22] Claudia Emde, Robert Buras-Schnell, Arve Kylling, Bernhard Mayer, Josef Gasteiger, Ulrich Hamann, Jonas Kylling, Bettina Richter, Christian Pause, Tim Dowling, et al. The libradtran software package for radiative transfer calculations (version 2.0. 1). *Geoscientific Model Development*, 9(5):1647–1672, 2016.

[23] Leonid G Sokoletsky, Vladimir P Budak, Fang Shen, and Alexander A Kokhanovsky. Comparative analysis of radiative transfer approaches for calculation of plane transmittance and diffuse attenuation coefficient of plane-parallel light scattering layers. *Applied optics*, 53(3):459–468, 2014.

[24] JW Hovenier and CVM Van der Mee. Fundamental relationships relevant to the transfer of polarized light in a scattering atmosphere. *Astronomy and Astrophysics*, 128:1–16, 1983.

[25] Steven Platnick. Vertical photon transport in cloud remote sensing problems. *Journal of Geophysical Research: Atmospheres*, 105(D18):22919–22935, 2000.

[26] Svetlana Y Kotchenova, Eric F Vermote, Raffaella Matarrese, and Frank J Klemm Jr. Validation of a vector version of the 6s radiative transfer code for atmospheric correction of satellite data. part i: Path radiance. *Applied optics*, 45(26):6762–6774, 2006.

[27] Subrahmanyan Chandrasekhar. *Radiative transfer*. Courier Corporation, 2013.

[28] PS Mudgett and LW Richards. Multiple scattering calculations for technology. *Applied Optics*, 10(7):1485–1502, 1971.

[29] Paul Kubelka and Franz Munk. An article on optics of paint layers. *Z. Tech. Phys*, 12(593-601), 1931.

[30] Lionel Simonot, Roger D Hersch, Mathieu Hébert, and Serge Mazauric. Multilayer four-flux matrix model accounting for directional-diffuse light transfers. *Applied optics*, 55(1):27–37, 2016.

[31] R Alcaraz de la Osa, A García Alonso, D Ortiz, F González, F Moreno, and JM Saiz. Extension of the kubelka–munk theory to an arbitrary substrate: a monte carlo approach. *JOSA A*, 33(10):2053–2060, 2016.

[32] Bruno Maheu, Jean-Noël Letoulouzan, and Gérard Gouesbet. Four-flux models to solve the scattering transfer equation in terms of lorenz-mie parameters. *Applied optics*, 23(19):3353–3362, 1984.

[33] János Schanda. *Colorimetry: understanding the CIE system*. John Wiley & Sons, 2007.

[34] Henry R Kang. Applications of color mixing models to electronic printing. *Journal of Electronic Imaging*, 3(3):276–288, 1994.

[35] Gaurav Sharma. Color fundamentals for digital imaging. *Digital color imaging handbook*, 20, 2003.

[36] Sofía Pérez-Villar, Juan Rubio, and Jose Luis Oteo. Study of color and structural changes in silver painted medieval glasses. *Journal of Non-Crystalline Solids*, 354(17):1833–1844, 2008.

[37] R Alcaraz de la Osa, A Fernández, Y Gutiérrez, D Ortiz, F González, F Moreno, and JM Saiz. The extended kubelka-munk theory and its application to colloidal systems. In *Third International Conference on Applications of Optics and Photonics*, volume 10453, page 104531F. International Society for Optics and Photonics, 2017.

[38] Ian Freestone, Nigel Meeks, Margaret Sax, and Catherine Higgitt. The lycurgus cup—a roman nanotechnology. *Gold bulletin*, 40(4):270–277, 2007.

[39] Neus G Bastús, Joan Comenge, and Víctor Puntes. Kinetically controlled seeded growth synthesis of citrate-stabilized gold nanoparticles of up to 200 nm: size focusing versus ostwald ripening. *Langmuir*, 27(17):11098–11105, 2011.

[40] Christoph Ziegler and Alexander Eychmüller. Seeded growth synthesis of uniform gold nanoparticles with diameters of 15- 300 nm. *The Journal of Physical Chemistry C*, 115(11):4502–4506, 2011.

[41] Petr Suchomel, Libor Kvitek, Robert Prucek, Ales Panacek, Avik Halder, Stefan Vajda, and Radek Zboril. Simple size-controlled synthesis of au nanoparticles and their size-dependent catalytic activity. *Scientific Reports*, 8(1):4589, 2018.

[42] Hendrik Christoffel Hulst and Hendrik C van de Hulst. *Light scattering by small particles*. Courier Corporation, 1957.

[43] Warren J Wiscombe. *Mie scattering calculations: Advances in technique and fast, vector-speed computer codes*. National Technical Information Service, US Department of Commerce, 1979.

[44] Kurt A Fuller. Scattering of light by coated spheres. *Optics letters*, 18(4):257–259, 1993.

[45] Michael I Mishchenko, Joachim W Hovenier, and Larry D Travis. *Light scattering by nonspherical particles: theory, measurements, and applications*. Elsevier, 1999.

[46] PC Waterman. Matrix formulation of electromagnetic scattering. *Proceedings of the IEEE*, 53(8):805–812, 1965.

[47] VV Varadan, Y Ma, and VK Varadan. Theoretical analysis of the acoustic response of suspended sediment for hebble. *Marine geology*, 66(1-4):267–276, 1985.

[48] L Tsang and JA Kong. Multiple scattering of electromagnetic waves by random distributions of discrete scatterers with coherent potential and quantum mechanical formalism. *Journal of Applied Physics*, 51(7):3465–3485, 1980.

[49] Michael I Mishchenko, Larry D Travis, and Andrew A Lacis. *Scattering, absorption, and emission of light by small particles*. Cambridge university press, 2002.

[50] William E Vargas and Gunnar A Niklasson. Forward average path-length parameter in four-flux radiative transfer models. *Applied optics*, 36(16):3735–3738, 1997.

[51] Claude Rozé, Thierry Girasole, Gérard Gréhan, Gérard Gouesbet, and Bruno Maheu. Average crossing parameter and forward scattering ratio values in four-flux model for multiple scattering media. *Optics communications*, 194(4-6):251–263, 2001.

[52] William E Vargas and Gunnar A Niklasson. Pigment mass density and refractive index determination from optical measurements. *Journal of Physics: Condensed Matter*, 9(7):1661, 1997.

[53] William E Vargas and Gunnar A Niklasson. Forward-scattering ratios and average pathlength parameter in radiative transfer models. *Journal of Physics: Condensed Matter*, 9(42):9083, 1997.

[54] Eugene Hecht. *Optics*. Pearson Education, 2016.

[55] H. J. Mcnicholas. Absolute methods in reflectometry. *Bureau of Standards Journal of Research*, 1(1):29, 1928.

APPENDIX A

LIGHT SCATTERING THEORIES REVIEW

A.1 Mie scattering theory

The Mie scattering theory is a rigorous mathematical theory which provides the solution to Maxwell's equations for the problem of light scattering by a sphere of arbitrary size and refractive index. The solution takes the form of an infinite series of vector spherical wave functions (VSWFs). The theory is developed in classical textbooks such as van de Hulst [42] and Bohren and Huffman [12]. In this section we review the scattering problem and the main results from this versatile theory.

The scattering problem is described as follows: a spherical particle within a linear, isotropic, homogeneous medium is illuminated by an *arbitrarily polarized* monochromatic plane wave, see fig. A.1.[1] The aim is to determine the value of the electromagnetic fields at all points.

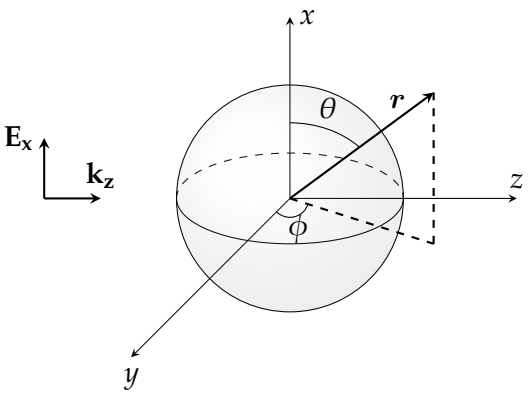

Figure A.1: Scheme of the scattering problem. A linearly polarized plane wave incident on a sphere of arbitrary size and refractive index.

The electric and magnetic field must satisfy the Maxwell equations and thus the following wave equations:

$$\begin{aligned} \nabla^2\mathbf{E} + k^2\mathbf{E} = 0\,, \\ \nabla^2\mathbf{H} + k^2\mathbf{H} = 0\,, \end{aligned} \tag{A.1}$$

where $k^2 = \omega^2\epsilon\mu$, ω is the angular frequency of electric and magnetic field, ϵ and μ the electric permittivity and magnetic permeability of the embedding medium. Both the electric and magnetic field are divergence-free and satisfy the following relationship:

$$\nabla \times \mathbf{E} = i\omega\mu\mathbf{H}\,, \qquad \nabla \times \mathbf{H} = -i\omega\epsilon\mathbf{E}\,, \tag{A.2}$$

The electric and magnetic field can be expanded as an infinite series of the VSWFs:

$$\mathbf{M} = \nabla \times \big(\mathbf{r}\psi\big), \qquad \mathbf{N} = \frac{\nabla \times \mathbf{M}}{k} \tag{A.3}$$

[1] Restricting ourselves to only plane waves does not lose generality of the problem since an arbitrary field can be decomposed into its Fourier components which are indeed plane waves.

where $\mathbf{r}$ is the radius vector and ϕ is a scalar field. The spherical vector harmonics are divergence-free and satisfy eq. (A.2) if the scalar field is a solution of the wave equation in polar coordinates

$$\frac{1}{r^2}\frac{\partial}{\partial r}\left(r^2\frac{\partial\psi}{\partial r}\right)+\frac{1}{r^2\sin\theta}\frac{\partial}{\partial\theta}\left(\sin\theta\frac{\partial\psi}{\partial\theta}\right)+\frac{1}{r^2\sin^2\theta}\frac{\partial^2\psi}{\partial\phi^2}+\mathbf{k}^2\psi=0\,. \tag{A.4}$$

The VSWFs generated by scalar fields that satisfy eq. (A.4) are

$$\mathbf{M_{emn}}=\nabla\times(\mathbf{r}\psi_{emn}), \qquad \mathbf{M_{omn}}=\nabla\times(\mathbf{r}\psi_{omn})\,, \tag{A.5}$$

$$\mathbf{N_{emn}}=\frac{\nabla\times\mathbf{M_{emn}}}{k}, \qquad \mathbf{N_{omn}}=\frac{\nabla\times\mathbf{M_{omn}}}{k}\,, \tag{A.6}$$

where

$$\psi_{emn}=\cos(m\phi)P_n^m(\cos\theta)z_n(kr)\,, \tag{A.7}$$

$$\psi_{omn}=\sin(m\phi)P_n^m(\cos\theta)z_n(kr)\,, \tag{A.8}$$

P_n^m is the associated Legendre polynomial of degree n and order m, z_n is any of the four Bessel functions j_n, y_n, $h_n^{(1)}$ or $h_n^{(2)}$.

A.1.1 Incident and Scattered Fields

The VSWFs constitute a complete base, hence the electric field and magnetic field can be expanded as an infinite series of the VSWFs. For example, the incident electric field can be written as

$$\mathbf{E_{inc}}=\sum_{m=0}^{\infty}\sum_{n=0}^{\infty}(B_{emn}\mathbf{M_{emn}}+B_{omn}\mathbf{M_{omn}}+A_{emn}\mathbf{N_{emn}}+A_{omn}\mathbf{N_{omn}})\,. \tag{A.9}$$

The A and B coefficients can be obtained by projecting the incident electric field the over every element of the base.

In the case of a linearly polarized plane wave in the x direction the eq. (A.9) reduces to

$$\mathbf{E_{inc}}=\sum_{n=0}^{\infty}E_n\left(\mathbf{M_{o1n}^{(1)}}-i\mathbf{N_{e1n}^{(1)}}\right), \tag{A.10}$$

where $E_n=i^nE_0(2n+1)/(n(n+1))$ and the superscript (1) states that the radial dependence is expressed in terms of the Bessel spherical function j_n. The corresponding magnetic field can be evaluated from eq. (A.2)

$$\mathbf{H_{inc}}=\frac{-k}{\omega\mu}\sum_{n=0}^{\infty}E_n\left(\mathbf{M_{e1n}^{(1)}}+i\mathbf{N_{o1n}^{(1)}}\right). \tag{A.11}$$

Applying the boundary condition between the sphere and the embedding medium we can obtain the electromagnetic field inside the sphere as well as the scattered.

$$(\mathbf{E_{inc}}+\mathbf{E_{sca}}-\mathbf{E_{int}})\times\hat{\mathbf{u}}_\mathbf{r}=(\mathbf{H_{inc}}+\mathbf{H_{sca}}-\mathbf{H_{int}})\times\hat{\mathbf{u}}_\mathbf{r}=0 \tag{A.12}$$

The scattered electric and magnetic fields are given by the following expressions

$$\mathbf{E_{sca}} = \sum_{n=1}^{\infty} E_n \left(i a_n \mathbf{N}_{e1n}^{(3)} - b_n \mathbf{M}_{o1n}^{(3)} \right) \tag{A.13}$$

$$\mathbf{H_{sca}} = \frac{k}{\omega \mu} \sum_{n=1}^{\infty} E_n \left(i b_n \mathbf{N}_{o1n}^{(3)} + a_n \mathbf{M}_{e1n}^{(3)} \right) \tag{A.14}$$

where the superscript (3) expresses that the radial dependence is specified by the spherical Hankel function $h_n^{(1)}$.

When the permeability of the particle equals the embedding medium's, the scattering coefficients are

$$\begin{aligned} a_n &= \frac{m\psi_n(mx)\psi_n'(x) - \psi_n(x)\psi_n'(mx)}{m\psi_n(mx)\xi_n'(x) - \xi_n(x)\psi_n'(mx)}, \\ b_n &= \frac{\psi_n(mx)\psi_n'(x) - m\psi_n(x)\psi_n'(mx)}{\psi_n(mx)\xi_n'(x) - m\xi_n(x)\psi_n'(mx)}, \end{aligned} \tag{A.15}$$

where $m = n/n_e$ is the relative refractive index, and $\psi_n(\rho) = \rho j_n(\rho)$ and $\xi_n(\rho) = \rho h_n^{(1)}(\rho)$ are the Riccatti-Bessel functions.

A.1.2 Cross Sections and Efficiency Factors

Relevant physical magnitudes can be derived from the scattered fields, e.g., the extinction, scattering and absorption cross sections. The cross sections in terms of the Mie coefficients are

$$C_{ext} = \frac{2\pi}{k^2} \sum_{n=1}^{\infty} (2n+1) \operatorname{Re}\{a_n + b_n\}, \tag{A.16}$$

$$C_{sca} = \frac{2\pi}{k^2} \sum_{n=1}^{\infty} (2n+1) \left(|a_n|^2 + \left|b_n\right|^2 \right), \tag{A.17}$$

$$C_{abs} = C_{ext} - C_{sca}, \tag{A.18}$$

A.1.3 Scattering Matrix

The scattered field series eq. (A.13) and eq. (A.14) are uniformly convergent and thus they can be truncated at a high order with negligible error. Using this truncation the transverse components of the electric scattered field are

$$E_{s\theta} \sim E_0 \frac{e^{ikr}}{-ikr} \cos\phi S_2(\mu) \tag{A.19}$$

$$E_{s\phi} \sim E_0 \frac{e^{ikr}}{-ikr} \sin\phi S_1(\mu), \tag{A.20}$$

with $\mu = \cos\theta$. Thus, the relationship between the incident and the scattered field amplitudes is

$$\begin{pmatrix} E_{\parallel sca} \\ E_{\perp sca} \end{pmatrix} = \frac{e^{i\mathbf{k}(\mathbf{r}-z)}}{-i\mathbf{kr}} \begin{pmatrix} S_2 & 0 \\ 0 & S_1 \end{pmatrix} \begin{pmatrix} E_{\parallel inc} \\ E_{\perp inc} \end{pmatrix}. \tag{A.21}$$

The scattering amplitudes in terms of the Mie coefficients are given by

$$S_1 = \sum_n \frac{2n+1}{n(n+1)}(a_n\pi_n + b_n\tau_n) \tag{A.22}$$

$$S_2 = \sum_n \frac{2n+1}{n(n+1)}(a_n\tau_n + b_n\pi_n) \tag{A.23}$$

where π_n and τ_n are the angle-dependent functions defined as follows

$$\pi_n = \frac{P_n^1}{\sin\theta} \qquad \tau_n = \frac{dP_n^1}{d\theta}\,, \tag{A.24}$$

and $P_n^m(\mu)$ is the Legendre function of first kind of degree n and order m.

From eq. (A.21) the Stokes scattering matrix which relates the standard Stokes parameters[2] of the incident field with the scattering field.

$$\begin{pmatrix} I_{sca} \\ Q_{sca} \\ U_{sca} \\ V_{sca} \end{pmatrix} = \frac{1}{\mathbf{k}^2\mathbf{r}^2} \begin{pmatrix} S_{11} & S_{12} & 0 & 0 \\ S_{12} & S_{11} & 0 & 0 \\ 0 & 0 & S_{33} & S_{34} \\ 0 & 0 & -S_{34} & S_{33} \end{pmatrix} \begin{pmatrix} I_{inc} \\ Q_{inc} \\ U_{inc} \\ V_{inc} \end{pmatrix}, \tag{A.25}$$

with

$$S_{11} = \frac{1}{2}\Big(|S_1|^2 + |S_2|^2\Big) \qquad S_{12} = \frac{1}{2}\Big(|S_2|^2 - |S_1|^2\Big)$$
$$S_{33} = \frac{1}{2}\Big(S_2^*S_1 + S_2S_1^*\Big) \qquad S_{34} = \frac{i}{2}\Big(S_1S_2^* - S_2S_1^*\Big).$$

The (1,1)-element is related to another practical magnitude, the phase function. The phase function is normalized with the following condition

$$\frac{1}{4\pi}\int_\Omega p(\mu)d\Omega = 1\,. \tag{A.26}$$

In the case of scattering by a sphere it is simply

$$\frac{1}{2}\int_0^\pi S_{11}(\cos\theta)\sin\theta\,\mathrm{d}\theta = 1\,. \tag{A.27}$$

A.1.4 Mie Scattering Code

To calculate absorption, scattering and extinction efficiencies (Q_{abs}, Q_{sca}, Q_{ext}) as well as the scattering amplitudes ($S_1(\theta)$, $S_2(\theta)$) we have implemented in python a Mie Scattering code following the procedure outlined in [43]. The code is provided in appendix B.

[2]Defined as in [12].

A.2 Beyond Mie Scattering Theory. T-Matrix Approach

Despite its broad applicability, Mie theory is limited as it is restricted to spherical, homogeneous, isotropic and non-magnetic particles in a non-absorbing medium. There have been many efforts in developing more advanced scattering theories to study other particles such as coated spheres [44], non-spherical particles [45], etc. A comprehensive review summarizing the theoretical as well as numerical extensions of the Mie Theory is provided in [14].

In this section we focus on a surface-based method extension, i.e., methods in which the boundary conditions are set on the particle's surface, the T-matrix method. This method, a.k.a., the null field method or the extended boundary condition method (EBCM), was first proposed by Waterman in 1965 [46] to compute electromagnetic scattering by an arbitrarily shaped, homogeneous particle. Owing to its potential it had a massive development in the subsequent decades and now it can be applied to the study of electromagnetic, acoustic, and elastodynamic wave scattering by sing and aggregated scatterers [47], multiple scattering in discrete random media [48], etc.

Among its advantages, the Mie theory is recovered in the limit of scattering by a homogeneous sphere, and its formalism in generalized spherical function enables efficient technique to compute orientation-averaged scattering properties.

A.2.1 T-matrix Ansatz

In this section we review briefly the ansatz of the T-matrix method. A more exhaustive description is performed in [49].

Let us analyze the scattering electromagnetic field due to an arbitrary finite scattering object illuminated by a plane wave. The scattering object can be either a single particle or a collection of aggregated particles. The T-matrix method is based on the expansion of both the incident and the scattered fields in terms of VSWFs:

$$\mathbf{E_{inc}}(\mathbf{r}) = \sum_{n=1}^{\infty}\sum_{m=-n}^{n}\left[a_{mn}\mathbf{M}^{(1)}_{mn}(k_1\mathbf{r}) + b_{mn}\mathbf{N}^{(1)}_{mn}(k_1\mathbf{r})\right], \tag{A.28}$$

$$\mathbf{E_{sca}}(\mathbf{r}) = \sum_{n=1}^{\infty}\sum_{m=-n}^{n}\left[p_{mn}\mathbf{M}^{(3)}_{mn}(k_1\mathbf{r}) + q_{mn}\mathbf{N}^{(3)}_{mn}(k_1\mathbf{r})\right], \qquad r > r_* \tag{A.29}$$

where k_1 is the wavenumber in the embedding medium and r_* is the radius of the smallest circumscribing sphere of the scatterer centered at the origin of the laboratory coordinate system.

As a consequence of the linearity of the Maxwell equations and the constitutive relations, the relationship between scattered-field and the incident-field coefficients is linear and is given by the transition matrix (T-matrix). Mathematically

$$\begin{pmatrix}\mathbf{p}\\ \mathbf{q}\end{pmatrix} = \mathbf{T}\begin{pmatrix}\mathbf{a}\\ \mathbf{b}\end{pmatrix} = \begin{pmatrix}T_{11} & T_{12}\\ T_{21} & T_{22}\end{pmatrix}\begin{pmatrix}\mathbf{a}\\ \mathbf{b}\end{pmatrix}. \tag{A.30}$$

Once the T-matrix is know the scattered field can be evaluated, and from the its relationship with the incident field the scattering amplitude matrix can be obtained, a general version

of eq. (A.21).

Furthermore, the orientation-averaged extinction and scattering cross sections can be evaluated from

$$C_{ext} = -\frac{1}{k_1^2|\mathbf{E}_{inc,0}|^2}\mathrm{Re}\left\{\sum_{n=1}^{\infty}\sum_{m=-n}^{n}\left[a_{mn}(p_{mn})^* + b_{mn}(q_{mn})^*\right]\right\} \tag{A.31}$$

$$C_{sca} = \frac{1}{k_1^2|\mathbf{E}_{inc,0}|^2}\sum_{n=1}^{\infty}\sum_{m=-n}^{n}\left[\left|p_{mn}\right|^2 + \left|q_{mn}\right|^2\right] \tag{A.32}$$

while the absorption cross section can be obtained from eq. (A.18).

A.2.2 T-matrix Algorithms

There are open-source scattering codes based on a T-matrix method available. In this work we have used a suite of MATLAB codes called SMARTIES (Spheroids Modeled Accurately with a Robust T-matrix Implementation for Electromagnetic Scattering). It allows for the calculation of the optical properties, such as absorption and scattering cross sections, of oblate and prolate spheroidal particles, [19].

APPENDIX B

MIE SCATTERING CODE

In this appendix we provide a python implementation of the Mie Scattering Theory following the guidelines proposed in [43].

```
import numpy as np
from scipy import special as sp


def miescattering(x,m,vAngles = None):
    vAngles = np.atleast_1d(vAngles)
    if (np.abs(m)*x<=0.1):
        # Mie coefficients in the small particle limits.
        N1 = 1. - (1./10.)*x**2 + ((4.*m**2 + 5.)/1400.)*x**4
        D1 = (m**2 + 2. + (1. - 7.*m**2/10.)*x**2 -
              ((8.*m**4 - 385.*m**2 + 350.)/1400.)*x**4 +
              (2j*((m**2 - 1.)/3.)*x**3)*(1. - (1./10.)*x**2))
        a1 = 2j*((m**2 - 1.)/3.)*(N1/D1)
        b1 = (1j*((m**2 - 1.)/45.)*x**2
              *((1.+((2.*m**2-5.)/70.)*x**2)/(1.-((2.*m**2-5.)/30.)*x**2)))
        a2 = (1j*((m**2 - 1.)/15.)*x**2
              *((1.-(1./14.)*x**2)/(2.*m**2+3.-((2.*m**2-7.)/14.)*x**2)))
        T = np.real((a1*np.conjugate(a1) + b1*np.conjugate(b1)
             + (5./3.)* a2*np.conjugate(a2)))

        # Efficiencies and asymmetry factors
        Qext = 6.*x*np.real(a1 + b1)+ (5./3.)*np.real(a2)
        Qsca = 6.*x**4*T
        Qabs = Qext -Qsca
        g = np.real(a1*np.conjugate(a2 + b1))/T

        # Scattering amplitudes
        if (np.all(vAngles != None)):
            ninety = 90. in vAngles
            mu = np.cos(np.radians(vAngles))
            S1p = (3./2.)*x**3*(a1 + (b1+(5./3.)*a2)*mu)
            S1n = (3./2.)*x**3*(a1 - (b1+(5./3.)*a2)*mu)
            S2p = (3./2.)*x**3*(b1 + a1*mu + (5./3.)*a2*(2.*mu**2-1.))
            S2n = (3./2.)*x**3*(b1 - a1*mu + (5./3.)*a2*(2.*mu**2-1.))

            if (ninety):
                S1 = np.append(S1p,S1n[(len(vAngles)-2)::-1])
                S2 = np.append(S2p,S2n[(len(vAngles)-2)::-1])
            else:
                S1 = np.append(S1p,S1n[::-1])
                S2 = np.append(S2p,S2n[::-1])
    else:
        # Nmax, upper limit term of the serie used to compute Mie coefficients
```

```
        if (x <= 8.):
            Nmax = int(x + 4.*x**(1./3.) + 1.)
        elif (8. < x and x < 4200.):
            Nmax = int(x + 4.05*x**(1./3.) + 2.)
        elif (4200. <= x):
            Nmax = int(x + 4.*x**(1./3.) + 2.)

        # Computation of the vectors phin, xin and An of length Nmax. (z = mx)
        # Functions sp.spherical_jn and sp.spherical_yn use up-recurrence:
        #   f_np1(x) = ((2n+1)/x)f_n(x) - f_nm1(x)
        def Phin(ini,fin,x):
            Phin = x*sp.spherical_jn(np.arange(ini,fin+1),x)
            return(Phin)

        def Xin(ini,fin,x):
            Xin = Phin(ini,fin,x)-1j*x*sp.spherical_yn(np.arange(ini,fin+1),x)
            return(Xin)

        phin = Phin(1,Nmax,x)
        phinm1 = Phin(0,Nmax-1,x)
        phinp1 = Phin(2,Nmax+1,x)

        xin = Xin(1,Nmax,x)
        xinm1 = Xin(0,Nmax-1,x)
        xinp1 = Xin(2,Nmax+1,x)


        # Computation of An.
        # Up-recurrence or down-recurrence condition
        def AnDownOrUP(mre):
            output = 16.35*mre**2 + 8.42*mre -15.04
            return output

        z = m*x
        if (np.abs(np.imag(m)) < AnDownOrUP(np.real(m))/x):
            # An computed by up-recurrence
            def tanZ(x,y):
                num = 2.*np.exp(2.*y)*np.sin(2.*x) + 1j*(np.exp(4.*y)-1.)
                den = 2.*np.exp(2*y)*np.cos(2.*x) + 1 + np.exp(4*y)
                return(num/den)

            def uprecurrenceAN(N,z):
                x = np.real(z)
                y = np.imag(z)
                An = np.zeros(N,dtype = np.complex)
                An[0] = -(1./z) + tanZ(x,y)/((1./z)*tanZ(x,y) - 1.)
                for i in range(1,N):
                    An[i] = -((i+1.)/z)+1./((i+1.)/z-An[i-1])
                return(An)

            An = uprecurrenceAN(Nmax,z)
            Anp1 = uprecurrenceAN(Nmax+1,z)[1:]

        else:
        # An computed by down-recurrence
            def LentzMethod(Nmax,x,m):
                ANmax = (Nmax + 1.)/(x*m)
```

```
    def ak(k):
        if (k == 1):
            ak = (Nmax + 1.)/(x*m)
        else:
            ak = (-1)**(k+1)*(2.*Nmax + 2.*k - 1.)/(x*m)
        return(ak)


    def nk(nkm1,k):
        nk = ak(k) + 1./nkm1
        return(nk)

    def dk(dkm1,k):
        dk = ak(k) + 1./dkm1
        return(dk)

    def nkIll(nkm1,k,nkIll):
        nk = ak(k) + nkm1/nkIll
        return(nk)

    def dkIll(dkm1,k,dkIll):
        dk = ak(k) + dkm1/dkIll
        return(dk)

    dkm1 = ak(2)
    nkm1 = nk(ak(1),2)

    maxIter = 5000
    epsilon1 = 1e-2
    epsilon2 = 1e-8
    ill = False

    for i in range(2,maxIter+1):
        if (i==maxIter+1):
            print('No convergence of An')
            break
        if (ill):
            ill = False
            continue
        if ((np.abs(nkm1/ak(i)) > epsilon1) and
            (np.abs(dkm1/ak(i)) > epsilon1)):
            t = nkm1/dkm1
            ANmax = ANmax*t
            if (np.abs(np.real(t)-1.) < epsilon2 and
                np.abs(np.imag(t)) < epsilon2):
                # Down-convergence
                break
            nkm1 = nk(nkm1,i+1)
            dkm1 = dk(dkm1,i+1)
        else:
            nkill = ak(i+1)*nkm1 + 1.
            dkill = ak(i+1)*dkm1 + 1.
            ANmax = ANmax*(nkill/dkill)
            nkm1 = nkill(nkm1,i+2,nkill)
            dkm1 = dkill(dkm1,i+2,dkill)
            ill = True

    return(ANmax)
```

```
160             def downrecurrenceAn(N,z):
                    An = np.zeros(N,dtype = np.complex)
                    An[0] = LentzMethod(N,x,m)
                    for i in range(0,N-1):
                        An[i+1] = (N-i)/z - 1./((N-i)/z + An[i])
165                 # to reverse the vector
                    An = An[::-1]
                    return(An)

                An = downrecurrenceAn(Nmax,z)
170             Anp1 = downrecurrenceAn(Nmax + 1,z)[1:]


        # Computation of an and bn, and an+1 and bn+1 for g factor
        nxinv = np.arange(1,Nmax+1)/x
175     nxinvp1 = np.arange(2,Nmax+2)/x
        n = np.arange(1,Nmax+1)

        an = ((An/m + nxinv)*phin - phinm1)/((An/m + nxinv)*xin - xinm1)
        bn = ((An*m + nxinv)*phin - phinm1)/((An*m + nxinv)*xin - xinm1)
180     anp1 = ((Anp1/m + nxinvp1)*phinp1 - phin)/((Anp1/m + nxinvp1)*xinp1
                - xin)
        bnp1 = ((Anp1*m + nxinvp1)*phinp1 - phin)/((Anp1*m + nxinvp1)*xinp1
                - xin)

185     # Efficiencies and asymmetry factors
        Qext = (2./x**2)*sum((2.*n+1.)*np.real(an + bn))
        Qsca = (2./x**2)*sum((2.*n+1.)*(np.real(an*np.conj(an)+bn*np.conj(bn))))
        Qabs = Qext - Qsca
        g = 4./(x**2*Qsca)*sum((n*(n + 2.)/(n + 1.))*np.real(an*np.conj(anp1)+
    bn*np.conj(bnp1)) + ((2.*n +1.)/(n*(n + 1.)))*np.real(an*np.conj(bn)))
190
        # Scattering amplitudes.
        if (np.all(vAngles!=None)):
            # Angular functions computation by up-recurrence
            def angularFunctionsUpR(theta,N):
195                 mu = np.cos(theta)
                    pin = np.zeros(N+2)
                    taun = np.zeros(N+1)
                    pin[1] = 1.
                    for n in range(1,N+1):
200                     s = mu*pin[n]
                        t = s - pin[n-1]
                        pin[n+1] = s + ((n+1.)/n)*t
                        taun[n] = (n+1.)*t-s
                    return pin[1:N+1],taun[1:]
205
            UangularFunctionsUpR = np.frompyfunc(angularFunctionsUpR,2,2)

            # Computation of S1 and S2
            def scatteringAmplitudes(an,bn,vAngles):
210                 ninety = 90. in vAngles
                    vAngles = np.radians(vAngles)
                    n = np.arange(1,len(an)+1)
                    factor = (2.*n + 1.)/(n*(n+1.))
                    sign = (-1)**(n+1)
215                 pin,taun = UangularFunctionsUpR(vAngles,len(an))
```

```
                Splusmu = np.zeros(len(vAngles),dtype=complex)
                Sminusmu = np.zeros(len(vAngles),dtype=complex)
                SplusmuN = np.zeros(len(vAngles),dtype=complex)
                SminusmuN = np.zeros(len(vAngles),dtype=complex)
                for i in range(len(vAngles)):
                    Splusmu[i] = sum(factor*(an+bn)*(pin[i]+taun[i]))
                    Sminusmu[i] = sum(factor*(an-bn)*(pin[i]-taun[i]))
                    SplusmuN[i] = sum(sign*factor*(an+bn)*(pin[i]-taun[i]))
                    SminusmuN[i] = sum(sign*factor*(an-bn)*(pin[i]+taun[i]))

                if (ninety):
                    S1 = np.append((1./2.)*(Splusmu+Sminusmu),
                                   ((1./2.)*(SplusmuN+SminusmuN))[(len(vAngles)
-2)::-1])
                    S2 = np.append((1./2.)*(Splusmu-Sminusmu),
                                   ((1./2.)*(SplusmuN-SminusmuN))[(len(vAngles)
-2)::-1])
                else:
                    S1 = np.append((1./2.)*(Splusmu+Sminusmu),
                                   ((1./2.)*(SplusmuN+SminusmuN))[::-1])
                    S2 = np.append((1./2.)*(Splusmu-Sminusmu),
                                   ((1./2.)*(SplusmuN-SminusmuN))[::-1])
                return S1,S2

            S1,S2 = scatteringAmplitudes(an,bn,vAngles)

    if (np.all(vAngles!=None)):
        # Angles at which the scattering amplitudes have been evaluated
        ninety = 90. in vAngles
        if (ninety):
            angles = np.append(vAngles,(180-vAngles)[(len(vAngles)-2)::-1])
        else:
            angles = np.append(vAngles,(180-vAngles)[::-1])
        return Qext,Qsca,Qabs,g,S1,S2,angles
    else:
        return Qext,Qsca,Qabs,g
```

APPENDIX C

FOUR-FLUX MODEL

C.1 Equations full derivation

In this appendix we provide a detailed derivation of the equations shown in section 3.2.

Differential equations solution

The solutions to eqs. (3.7) and (3.8) are easily obtained by direct integration and are given in eqs. (3.11) and (3.12). In order to solve eqs. (3.9) and (3.10), they first need to be decoupled. Following [32], we compute the derivative of the sum and subtraction of eqs. (3.9) and (3.10)

$$\begin{aligned}\frac{\mathrm{d}^2(J_d + I_d)}{\mathrm{d}z^2} &= \xi^2\beta[\beta + 2(1-\sigma_d)\alpha](J_d + I_d) \\ &\quad - \xi[\beta + 2(1-\sigma_d)\alpha]\alpha(J_c + I_c) \\ &\quad + (1-2\sigma_c)\alpha\zeta(J_c + I_c)\end{aligned} \tag{C.1}$$

$$\begin{aligned}\frac{\mathrm{d}^2(J_d - I_d)}{\mathrm{d}z^2} &= \xi^2\beta[\beta + 2(1-\sigma_d)\alpha](J_d + I_d) \\ &\quad + \xi\beta(1-2\sigma_c)\alpha(J_c - I_c) \\ &\quad - \alpha\zeta[J_c - I_c].\end{aligned} \tag{C.2}$$

Adding and subtracting eqs. (C.1) and (C.2) and substituting eqs. (3.11) and (3.12) we obtain second order decoupled differential equations

$$-\frac{\mathrm{d}^2 J_d}{\mathrm{d}z^2} + A^2 J_d = Bc_2\mathrm{e}^{\zeta z} + Cc_1\mathrm{e}^{-\zeta z} \tag{C.3}$$

$$-\frac{\mathrm{d}^2 I_d}{\mathrm{d}z^2} + A^2 I_d = Cc_2\mathrm{e}^{\zeta z} + Bc_1\mathrm{e}^{-\zeta z}\,. \tag{C.4}$$

where $\zeta = \alpha + \beta$ is the extinction coefficient per unit length and

$$A = \xi\sqrt{\beta[\beta + 2\alpha(1-\sigma_d)]} \tag{C.5}$$

$$B = \alpha[\xi\beta\sigma_c + \xi\alpha(1-\sigma_d) + \zeta\sigma_c] \tag{C.6}$$

$$C = \alpha\{\xi[\alpha(1-\sigma_d) + \beta(1-\sigma_c)] - \zeta(1-\sigma_c)\} \tag{C.7}$$

Applying standard procedures to solve differential equations we obtain eqs. (3.13) and (3.14), where the following relationships hold

$$c_5 = \frac{Bc_2}{A^2 - \zeta^2} \tag{C.8}$$

$$c_6 = \frac{Cc_1}{A^2 - \zeta^2} \tag{C.9}$$

$$c_9 = \frac{Cc_2}{A^2 - \zeta^2} \tag{C.10}$$

$$c_{10} = \frac{Bc_1}{A^2 - \zeta^2} \tag{C.11}$$

Initially there are four first order differential equations hence only four c_i coefficients are independent. We can derive expressions for c_7 and c_8 in terms of c_3 and c_4. First, we substitute eqs. (3.11) to (3.14) in eq. (3.10) and regroup

$$\begin{aligned}0 = &\sinh(Az)[\xi(\beta + \alpha(1-\sigma_d))c_4 + \xi(1-\sigma_d)\alpha c_8 - Ac_3] \\ &+ \cosh(Az)[\xi(\beta + \alpha(1-\sigma_d))c_3 + \xi(1-\sigma_d)\alpha c_7 - Ac_4] \\ &+ \mathrm{e}^{\zeta z}[\xi(\beta + \alpha(1-\sigma_d))c_5 + \xi(1-\sigma_d)\alpha c_9 - \sigma_c \alpha c_2 - \zeta c_5] \\ &+ \mathrm{e}^{-\zeta z}[\xi(\beta + \alpha(1-\sigma_d))c_6 + \xi(1-\sigma_d)\alpha c_{10} - (1-\sigma_c)\alpha c_1 - \zeta c_6].\end{aligned}$$

Isolating c_7 and c_8 from the first two terms:

$$c_7 = \frac{Dc_3 - Ac_4}{E} \tag{C.12}$$

$$c_8 = \frac{Dc_4 - Ac_3}{E}\,. \tag{C.13}$$

and

$$D = \xi[\beta + \alpha(1-\sigma_d)] \tag{C.14}$$

$$E = \xi\alpha(1-\sigma_d) = D - \xi\beta, \tag{C.15}$$

To find exact solutions we use the boundary conditions. The boundary conditions at the interface $z = 0$ are

$$I_c(0) = (1 - r_{c12})fI + r_{c12}J_c(0) \tag{C.16}$$

$$I_d(0) = (1 - r_{d12})(1-f)I - r_{d21}J_d(0), \tag{C.17}$$

where I is the incident light intensity. The boundary conditions at $z = h$ are

$$J_c(h) = R_{sc}I_c(h) \tag{C.18}$$

$$J_d(h) = R_{sd}I_d(h). \tag{C.19}$$

where R_{sc} and R_{sd} are the multiple boundary reflections at the substrate,i.e., the effective reflection coefficients for collimated and diffuse radiation at the film-substrate interface,

$$R_{sc} = \frac{r_{c23}(1 - 2r_{c34}\tau_c^2) + r_{c34}\tau_c^2}{1 - r_{c23}r_{c34}\tau_c^2}, \tag{C.20}$$

$$R_{sd} = \frac{r_{d23} + (1 - r_{d23} - r_{d32})r_{d34}\tau_d^2}{1 - r_{d32}r_{d34}\tau_d^2}, \tag{C.21}$$

where τ_c and τ_d are the internal transmittance coefficients, i.e., the fraction of light that traverses the substrate without being absorbed, for collimated and diffuse light respectively.

Substituting eqs. (3.11) and (3.12) in eqs. (C.16) and (C.18) and isolating

$$c_1 = \frac{(1 - r_{c12})fI}{1 - r_{c12}R_{sc}\mathrm{e}^{-2\zeta h}} \tag{C.22}$$

$$c_2 = \frac{(1 - r_{c12})fIR_{sc}\mathrm{e}^{-2\zeta h}}{1 - r_{c12}R_{sc}\mathrm{e}^{-2\zeta h}}. \tag{C.23}$$

Likewise, expressions for c_3 and c_4 are found substituting eqs. (3.13) and (3.14) in eqs. (C.17) and (C.19). After some lengthy but straight-forward algebra we find

$$c_3 = \sigma_1 fI + \sigma_2(1-f)I \tag{C.24}$$
$$c_4 = \sigma_3 fI + \sigma_4(1-f)I, \tag{C.25}$$

where

$$\begin{aligned}\sigma_1 = &\Big\{\Big[A[(C+BR_{sc}) - R_{sd}(B+CR_{sc})]\mathrm{e}^{-\zeta h}\Big] \\ &+ [AR_{sd}\cosh(Ah) + (E - R_{sd}D)\sinh(Ah)] \\ &\times \Big[(C - r_{d21}B)R_{sc}\mathrm{e}^{-2\zeta h} + (B - r_{d21}C)\Big]\Big\} \\ &\times (1 - r_{c12})\Big[(1 - r_{c12}R_{sc}\mathrm{e}^{-2\zeta h})(A^2 - \zeta^2)DEN\Big]^{-1}\end{aligned} \tag{C.26}$$

$$\sigma_2 = \frac{(r_{d12}-1)[AR_{sd}\cosh(Ah) + (E - R_{sd}D)\sinh(Ah)]}{DEN} \tag{C.27}$$

$$\begin{aligned}\sigma_3 = &\Big\{\Big[(D - r_{d21}E)\left[(C+BR_{sc}) - R_{sd}(B+CR_{sc})\right]\mathrm{e}^{-\zeta h}\Big] \\ &- [(E - R_{sd}D)\cosh(Ah) + AR_{sd}\sinh(Ah)] \\ &\times \Big[(C - r_{d21}B)R_{sc}\mathrm{e}^{-2\zeta h} + (B - r_{d21}C)\Big]\Big\} \\ &\times (1 - r_{c12})\Big[(1 - r_{c12}R_{sc}\mathrm{e}^{-2\zeta h})(A^2 - \zeta^2)DEN\Big]^{-1}\end{aligned} \tag{C.28}$$

$$\sigma_4 = \frac{(1-r_{d12})[(E - R_{sd}D)\cosh(Ah) + AR_{sd}\sinh(Ah)]}{DEN}. \tag{C.29}$$

Reflectance, Transmittance, Absorptance and Transverse Energy Density

The total reflectance has an specular and a diffuse contribution. The specular contribution is the ratio of collimated reflected intensity to the total incident intensity

$$\mathcal{R}_c = \frac{r_{c12}fI + (1 - r_{c12})J_c(0)}{I}. \tag{C.30}$$

Substituting eqs. (3.12) and (C.23) in eq. (C.30), eq. (3.17) is obtained. Analogously, the diffuse contribution

$$\mathcal{R}_d = \frac{r_{d12}(1-f)I + (1 - r_{d21})J_d(0)}{I}. \tag{C.31}$$

Substituting eqs. (3.13), (C.8), (C.9), (C.22) and (C.24) in eq. (C.31) and isolating the contribution from the collimated and diffuse incident light we obtain eqs. (3.18) and (3.19), where

$$C_0 = A[(C + BR_{sc}) - R_{sd}(B + CR_{sc})] \tag{C.32}$$

$$\begin{aligned}C_1 = &[A(BR_{sd} - C)\cosh(Ah) \\ &+ [B(E - DR_{sd}) + C(ER_{sd} - D)]\sinh(Ah)]\end{aligned} \tag{C.33}$$

$$\begin{aligned}C_2 = &R_{sc}[A(CR_{sd} - B)\cosh(Ah) \\ &+ [C(E - DR_{sd}) + B(ER_{sd} - D)]\sinh(Ah)]\end{aligned} \tag{C.34}$$

As well as the reflectance, the transmittance has also an specular and a diffuse contribution. In this case, the specular (diffuse) contribution is given by the sum of all the transmitted collimated (diffuse) rays originated due to multiple reflections within the substrate divided by the total incident intensity.

$$\mathcal{T}_c = T_{sc}\frac{I_c(h)}{I} = [\frac{(1-r_{c23})(1-r_{c34})\tau_c}{(1-r_{c23}r_{c34}\tau_c^2)}]\frac{I_c(h)}{I} \tag{C.35}$$

$$\mathcal{T}_d = T_{sd}\frac{I_d(h)}{I} = [\frac{(1-r_{d23})(1-r_{d34})}{1-r_{d32}r_{d34}\tau_d^2}]\frac{I_d(h)}{I}. \tag{C.36}$$

Substituting eq. (3.11) in eq. (C.35) and eq. (3.14) in eq. (C.36) and isolating the different contributions we get eqs. (3.20) to (3.22), where

$$D_1 = A\left[(r_{d21}C - B) + R_{sc}(r_{d21}B - C)\right] \tag{C.37}$$

$$D_2 = (E - r_{d21}D)(C + BR_{sc}) - (D - r_{d21}E)(B + CR_{sc}) \tag{C.38}$$

$$D_3 = A(B - r_{d21}C) \tag{C.39}$$

$$D_4 = AR_{sc}(C - r_{d21}B). \tag{C.40}$$

We have derived new expressions to evaluate the substrate's contribution to the total absorptance and therefore, a method to evaluate the different absorptance contributions. The system's total absorptance is simply the amount of light that is neither reflected nor transmitted. Mathematically is given by

$$\mathcal{A} = 1 - \mathcal{R} - \mathcal{T}. \tag{C.41}$$

Light can be absorbed either at the film or at the substrate. Thus, $\mathcal{A}$ can be rewritten as

$$\mathcal{A} = \mathcal{A}_f + \mathcal{A}_s = \mathcal{A}_f + f\mathcal{A}_{sc} + (1-f)\mathcal{A}_{sd}, \tag{C.42}$$

The absorption at the substrate, $\mathcal{A}_s$, can be evaluated from

$$\mathcal{A}_s = \frac{A_d I_d(h) + A_c I_c(h)}{I}, \tag{C.43}$$

where A_d and A_c are the diffuse and collimated light absorbed inside the substrate, given by

$$\begin{aligned} A_d &= 1 - R_{sd} - T_{sd} \\ &= \frac{(1-r_{d23})(1-\tau_d) + r_{d34}\tau_d(1-\tau_d - r_{d23}\tau_d)}{1-r_{d32}r_{d34}\tau_d^2} \end{aligned} \tag{C.44}$$

$$\begin{aligned} A_c &= 1 - R_{sc} - T_{sc} \\ &= \frac{(1-r_{c23})(1-\tau_c) + r_{c34}\tau_c(1-\tau_c - r_{c23}\tau_c)}{1-r_{c23}r_{c34}\tau_c^2}. \end{aligned} \tag{C.45}$$

Substituting eqs. (3.11), (3.14), (C.44) and (C.45) in eq. (C.43), we obtain

$$\begin{aligned} \mathcal{A}_{sc} = &\frac{(1-r_{c12})[D_1\cosh(Ah) + D_2\sinh(Ah) + D_3 e^{\zeta h} + D_4 e^{-\zeta h}]}{(1-r_{c12}R_{sc}e^{-2\zeta h})(A^2-\zeta^2)DEN} \\ &+ \frac{[(1-r_{c23})(1-\tau_c) + r_{c31}\tau_c(1-\tau_c - r_{c23} + r_{c23}\tau_c)](1-r_{c12}e^{-\zeta h})}{(1-r_{c23}r_{c34}\tau_c^2)(1-r_{c12}R_{sc}e^{-2\zeta h})} \end{aligned} \tag{C.46}$$

$$\mathcal{A}_{sd} = -\frac{[(1-r_{d23})(1-\tau_d) + r_{d34}\tau_d(1-\tau_d - r_{d23}\tau_d)](1-r_{d12})A}{(1-r_{d32}r_{d34}\tau_d^2)DEN}. \tag{C.47}$$

The total light intensity at a given z can be easily evaluated from the sum of all fluxes which can be associated to the transverse energy density $\mathcal{U}(z)$

$$\mathcal{U}(z) = I_c(z) + I_d(z) + J_c(z) + J_d(z). \tag{C.48}$$

C.2 Parameters of the Four-Flux Model

The four-flux model requires many parameters whose values are not trivial. Thus in this appendix we review the physics behind each of them.

Average pathlength parameter

The average pathlength parameter ξ, also known as the average crossing parameter, provides the relative distance traveled by the diffuse light compared to collimated light. The value of ξ follows from its definition for two specific cases: under collimated radiation $\xi = 1$ and under perfectly diffuse incident radiation $\xi = 2$. However, ξ does not have to be constant. Mathematically, a light beam, whose direction forms an angle θ with the z-axis, travels a distance ΔL which is $1/\cos\theta$ larger than Δz, the distance traveled by a collimated beam. Averaging both sides over the intensity radiation field and integrating over the forward hemisphere the average pathlength can be evaluated with

$$\xi(z) = \frac{\int_0^1 I\big(z,\mu\big)\,\mathrm{d}\mu}{\int_0^1 \mu I\big(z,\mu\big)\,\mathrm{d}\mu}\,. \tag{C.49}$$

Due to the difficulty in evaluating eq. (C.49) it has usually been considered constant [32] or as a fitting parameter. In certain cases there are explicit formulae for ξ, e.g., in the case of films containing spherical particles in a nonabsorbing matrix [50], in other cases its value has been studied with numerical methods [51]. We have set this parameter to $\xi = 2$ to avoid complications.

Scattering and absorption coefficients per unit length

The relative energy lost by a collimated beam flowing perpendicularly to an infinitesimal slab $\mathrm{d}z$ due to scattering (absorption) is related to the scattering (absorption) coefficient by $\alpha\,\mathrm{d}z$ ($\beta\,\mathrm{d}z$). In general, α and β depend on the properties of the material and are usually phenomenological parameters. In the case of a nonabsorbing medium with homogeneous spherical inclusions α and β can be evaluated from Mie-Lorenz theory

$$\alpha = \frac{f}{V} C_{\mathrm{sca}} = \rho_n C_{\mathrm{sca}}\,, \tag{C.50}$$

$$\beta = \frac{f}{V} C_{\mathrm{abs}} = \rho_n C_{\mathrm{abs}}\,, \tag{C.51}$$

where f is the filling fraction, V is the particle volume, ρ_n is the particle number density, and C_{sca} and C_{abs} are the scattering and absorption cross sections of the inclusions [52].

Forward scattering ratios

The forward scattering ratio is simply the relative amount of light scattered in the forward hemisphere within the media. This value is different for collimated (σ_c) and diffuse light (σ_d). In the case of collimated light, σ_c equals the amount of light scattered in the forward direction over the total scattered light, which can be evaluated using

$$\sigma_c = \frac{\int_0^1 p(\mu)\,\mathrm{d}\mu}{\int_{-1}^1 p(\mu)\,\mathrm{d}\mu}, \tag{C.52}$$

where $p(\mu)$ is the phase function. In the case of diffuse light the evaluation is more cumbersome since the forward hemisphere with respect to the beam direction does not coincide with the medium's forward hemisphere.

$$\sigma_d = \frac{\int_0^{\pi/2} \sigma(\alpha)\sin(2\alpha)\,\mathrm{d}\alpha}{\int_0^{\pi/2} \sin(2\alpha)\,\mathrm{d}\alpha} = \int_0^{\pi/2} \sigma(\alpha)\sin(2\alpha)\,\mathrm{d}\alpha \tag{C.53}$$

σ_d is commonly evaluated numerically but there are analytical expressions for specific cases, e.g., a non-absorbing medium with absorbing-scattering particles [53].

The assumption that $\sigma_c = \sigma_d$ has been made in all calculations of chapter 3, [32], while it has been numerically evaluated using eq. (C.53) in chapter 5's calculations. The former approximation does not hold except for limiting cases such as isotropic scattering. We have assumed this configuration so the values $\sigma_c = \sigma_d = 0.5$ have been used in all the computations.

Reflectances at the interfaces

Usually we have information relative to the refractive indices of the different media rather than the reflectances at each interface. However, these magnitudes are easily related by the Fresnel equation. The reflectance at the interface between medium i and medium j for a light beam with angle of incidence θ_i is

$$r_s(\theta_i) = \left|\frac{n_j\cos\theta_i - n_i\cos\theta_j}{n_j\cos\theta_i + n_i\cos\theta_j}\right|^2 \tag{C.54}$$

for parallel polarization and

$$r_p = \left|\frac{n_j\cos\theta_j - n_i\cos\theta_i}{n_j\cos\theta_j + n_i\cos\theta_i}\right|^2 \tag{C.55}$$

for perpendicular polarization, where n_i and n_j are the refractive indices of the media and θ_j is the angle of refraction which can be evaluated using the Snell law [54]. For unpolarized collimated light the reflectance at the interface is

$$r_{cij} = \frac{1}{2}\left(r_s + r_p\right) \tag{C.56}$$

with $\theta_i = \theta_p = 0$. In the case of diffuse light, multiple incident directions have to be taken into account. Therefore, we average the Fresnel factors over all possible angles of incidence [55]

$$r_{dij} = \frac{1}{2}\int_0^{\pi/2} [r_s(\alpha) + r_p(\alpha)] \sin(2\alpha)\, \mathrm{d}\alpha \tag{C.57}$$

Transmittances across the substrate

In addition to the absorption within the film, there can be absorption in the substrate. The substrate's absorption can be characterize by the transmittance τ across the substrate, i.e., the fraction of light that crosses the substrate without being absorbed. Since diffuse light covers more distance to travel the same distance than collimated light, $\tau_d \neq \tau_c$. The transmittance of a material is related to the attenuation coefficient, $\alpha(z)$, by the following expression

$$\tau = \exp\left(-\int_0^l \alpha(z)\, \mathrm{d}z\right), \tag{C.58}$$

where l is the material's length. Assuming constant attenuation over the whole substrate, i.e., a constant attenuation coefficient, the substrate's internal collimated and diffuse transmittances are related by

$$\tau_d = \tau_c^{\xi}\,. \tag{C.59}$$

We have applied this relationship throughout all the paper.

C.3 Monte Carlo Algorithm

Algorithm 1 Four-flux Monte Carlo.

▷ Each incoming beam is initially moving to the right

while moving **do**
  $\rho \leftarrow$ uniformly distributed random number $\in (0, 1)$
  if collimated **then**
    if $\rho < PK^{\mathrm{col}}$ **then** ▷ beam absorbed
      beam absorbed
      STOP
    else if $\rho < (PK^{\mathrm{col}} + PR)$ **then** ▷ beam back-reflected
      if moving to the right **then**
        if first layer **then**
          beam reflected (specular)
          STOP
        else
          reverse direction
          back one layer
      else
        reverse direction
        move one layer
    else if $\rho < (PK^{\mathrm{col}} + PR + PS^{\mathrm{col}}_{\mathrm{back}})$ **then** ▷ beam back-scattered

if moving to the right **then**
if first layer **then**
beam reflected (diffuse)
STOP
else
reverse direction
back one layer
collimated = false
else
reverse direction
move one layer
collimated = false
else if $\rho < (PK^{\text{col}} + PR + PS^{\text{col}}_{\text{back}} + PS^{\text{col}}_{\text{forward}})$ **then** ▷ beam forward-scattered
if moving to the right **then**
if last layer **then**
beam transmitted (diffuse)
STOP
else
move one layer
collimated = false
else
if first layer **then**
beam reflected (diffuse)
STOP
else
back one layer
collimated = false
else ▷ beam travels through
if moving to the right **then**
if last layer **then**
beam transmitted (specular)
STOP
else
move one layer
else
if first layer **then**
beam reflected (specular)
STOP
else
back one layer
else
same as two-flux [31]

APPENDIX D

CIE COLORIMETRY

D.1 Color Spaces Conversions

In this appendix the equations needed to perform the color space conversions that have been made in this work. This topic is covered more extensively in [33].

D.1.1 From XYZ to RGB

The conversion from RGB to XYZ can be expressed in matricial form

$$\begin{bmatrix} X \\ Y \\ Z \end{bmatrix} = \mathbf{M} \begin{bmatrix} R \\ G \\ B \end{bmatrix} \tag{D.1}$$

where **M** is a 3*x*3 matrix with different values depending on the CIE observer:

$$\mathbf{M} = \begin{bmatrix} 2.768892 & 1.751748 & 1.130160 \\ 1.000000 & 4.590700 & 0.060100 \\ 0 & 0.056508 & 5.594292 \end{bmatrix} \tag{D.2}$$

$$\mathbf{M} = \begin{bmatrix} 0.341080 & 0.189145 & 0.387529 \\ 0.139058 & 0.837460 & 0.073160 \\ 0 & 0.039553 & 1.026200 \end{bmatrix} \tag{D.3}$$

Equation (D.2) and eq. (D.3) in the case of the 1931 and 1964 CIE observers respectively.

D.1.2 From XYZ to Lab

The L*a*b* coordiantes are related to the tristimulus values by

$$L^* = 116 f_y - 16\,, \tag{D.4}$$

$$a^* = 500\Big(f_x - f_y\Big)\,, \tag{D.5}$$

$$b^* = 200\Big(f_y - f_z\Big)\,, \tag{D.6}$$

where

$$f_x = \begin{cases} (x_r)^{1/3} & \text{if } x_r > \epsilon \\ \dfrac{\kappa x_r + 16}{116} & \text{otherwise} \end{cases} \quad f_y = \begin{cases} \Big(y_r\Big)^{1/3} & \text{if } y_r > \epsilon \\ \dfrac{\kappa y_r + 16}{116} & \text{otherwise} \end{cases} \quad f_z = \begin{cases} (z_r)^{1/3} & \text{if } z_r > \epsilon \\ \dfrac{\kappa z_r + 16}{116} & \text{otherwise} \end{cases} \tag{D.7}$$

where $i_r = I/I_r$ and (X_r, Y_r, Z_r) are the tristimulus values of a reference white, $\epsilon = 216/24389$ and $\kappa = 24389/27$ are the parameters that map relative luminance Y_r into lightness L^*.

D.1.3 From Lab to LCh

The CIELCh coordinates are related to CIELab coordinates by

$$L = L \tag{D.8}$$

$$C = \sqrt{a^2 + b^2}, \tag{D.9}$$

$$h^\circ = \arctan\left(\frac{b}{a}\right), \tag{D.10}$$

D.2 Color Difference CIEDE00

Given two colors, color 1 and color 2, characterized by the trichromatic coordinates (L_1, a_1, b_1) and (L_2, a_2, b_2) respectively, the color difference given by the CIEDE00 is:

$$\Delta E_{00} = \sqrt{\left(\frac{\Delta L'}{K_L S_L}\right)^2 + \left(\frac{\Delta C'}{K_C S_C}\right)^2 + \left(\frac{\Delta H'}{K_H S_H}\right)^2 + R_T\left(\frac{\Delta C'}{K_C S_C}\right)\left(\frac{\Delta H'}{K_H S_H}\right)}, \tag{D.11}$$

where

$$\bar{L}' = \frac{L_1 + L_2}{2}$$

$$C_1 = \sqrt{a_1^2 + b_1^2}$$

$$C_2 = \sqrt{a_2^2 + b_2^2}$$

$$\bar{C} = \frac{C_1 + C_2}{2}$$

$$G = \frac{1}{2}\left(1 - \sqrt{\frac{\bar{C}^7}{\bar{C}^7 + 25^7}}\right)^2$$

$$a_1' = a_1(1 + G)$$

$$a_2' = a_2(1 + G)$$

$$C_1' = \sqrt{a_1'^2 + b_1^2}$$

$$C_2' = \sqrt{a_2'^2 + b_2^2}$$

$$\bar{C}' = \frac{C_1' + C_2'}{2}$$

$$\Delta L' = L_2 - L_1$$

$$\Delta C' = C_2' - C_1'$$

$$S_L = 1 + \frac{0.015\left(\bar{L}' - 50\right)^2}{\sqrt{20 + \left(\bar{L}' - 50\right)^2}}$$

$$S_C = 1 + 0.045\bar{C}'$$

$$S_H = 1 + 0.015\bar{C}'T$$

$$K_L = K_C = K_H = 1 \qquad \text{default}$$

$$h_1' = \begin{cases} \arctan\left(\frac{b_1}{a_1'}\right) & \text{if } \arctan\left(\frac{b_1}{a_1'}\right) \geq 0 \\ \arctan\left(\frac{b_1}{a_1'}\right) + 360^\circ & \text{otherwise} \end{cases}$$

$$h_2' = \begin{cases} \arctan\left(\frac{b_2}{a_2'}\right) & \text{if } \arctan\left(\frac{b_2}{a_2'}\right) \geq 0 \\ \arctan\left(\frac{b_2}{a_2'}\right) + 360^\circ & \text{otherwise} \end{cases}$$

$$\bar{H}' = \begin{cases} \left(\frac{h_1' + h_2' + 360^\circ}{2}\right) & \text{if } \left|h_1' + h_2'\right| > 180^\circ \\ \left(\frac{h_1' + h_2'}{2'}\right) & \text{otherwise} \end{cases}$$

$$\Delta H' = 2\sqrt{C_1' C_2'}\sin(\Delta h'/2)$$

$$\Delta\bar{h}' = \begin{cases} h_2' - h_1' & \text{if } \left|h_2' - h_1'\right| \leq 180^\circ \\ h_2' - h_1' + 360^\circ & \text{if } \left|h_2' - h_1'\right| > 180^\circ \text{and } h_2' \leq h_1' \\ h_2' - h_1' - 360^\circ & \text{otherwise} \end{cases}$$

$$T = 1 - 0.17\cos(\bar{H}' - 30^\circ) + 0.24\cos(2\bar{H}') + 0.32\cos(3\bar{H}' + 6^\circ) + 0.20\cos(4\bar{H}' - 63^\circ)$$

$$\Delta\theta = 30\exp\left(-\left(\frac{\bar{H}' - 275^\circ}{25}\right)^2\right)$$

$$R_C = 2\sqrt{\frac{\bar{C}'^7}{\bar{C}'^7 + 25^7}}$$

$$R_T = -R_C\sin(2\theta)$$